Background ambient atmospheric mercury concentrations for the South African interior

L Bredenkamp

orcid.org/0000-0003-1559-8239

Dissertation accepted in fulfilment of the requirements for the degree *Master of Science in Environmental Sciences* at the North-West University

Supervisor:	Prof JP Beukes
Co-Supervisor:	Prof PG van Zyl

Graduation May 2021

23488697

Acknowledgements

I would like to express my heartfelt gratitude and appreciation towards the following individuals and entities:

- Blessed is Yahweh my Elohim for giving me the strength to persevere and complete this study,
- My supervisors and mentors, Prof. Paul Beukes and Prof. Pieter van Zyl for their guidance, patience and motivation throughout the course of the study, both on a personal and professional level,
- Dr Micky Josipovic and the entire team at Welgegund for helping to maintain the Tekran® analyser in good shape,
- Mr Andrew Fouché for assistance in ordering the consumables used throughout the study,
- My mother, Linda, and late father, Stephan, for their unconditional love and support, and for instilling a spirit of perseverance in me from a young age,
- My husband, PW, for your loving support and understanding, even whilst completing your own M.Sc. study,
- My son, Joshua, for always putting a smile on my face after a long day,
- My in-laws, Hein and Santa, for your continued encouragement,
- The candidate also hereby expresses their sincerest gratitude towards SASOL Group Technology, Sasolburg for providing partial funding and the ambient mercury vapour analyser for this study.

Abstract

Atmospheric mercury (Hg) pollution is a global health concern. Once emitted into the atmosphere, gaseous elemental mercury (Hg^0) can be converted to highly reactive gaseous oxidised mercury (Hg^{2+}), which is deposited to the earth's surface. In aquatic environments Hg^{2+} is converted to methylmercury (MeHg) which is toxic, has the ability to bioaccumulate along the food chain and ultimately causes very serious medical conditions in humans. During this study continuous total gaseous mercury (TGM) measurements were conducted at Welgegund, a regional background site situated in the South African interior, from 17 September 2016 to 5 May 2017. The average TGM concentration measured over the study period was 1.68 ± 0.94 $ng.m^{-3}$. This value compared well with data from most other measurement sites in South Africa, but was about twice as high as measurements from international, remote background sites. A clear diurnal trend was identified and attributed to the oxidation of Hg by ozone (O_3) and the associated hydroxyl radical ($OH^{\bullet}$), as well as the evolution of the planetary boundary layer (PBL). The diurnal profile also indicated transport of Hg from more distant sources to Welgegund. Furthermore, a seasonal trend could be recognised which was driven mostly by regional open biomass burning as an additional source in the dry season and enhanced wet deposition in the wet season. An overlay back trajectory map revealed three main air mass fetch regions for Welgegund during the study period, each with a unique mean hourly TGM concentration range associated to it. The TGM concentration range for each fetch region was dependent on the population density, point sources, ozone concentration, biomes and biomass burning events therein.

Key words: Atmospheric mercury (Hg), total gaseous mercury (TGM), Welgegund, temporal and spatial patterns, South African interior.

Table of Contents

List of Figures (abbreviated)

List of Tables

CHAPTER 1

Introduction

This chapter briefly describes the status of atmospheric mercury (Hg) pollution and associated legislation in South Africa. Knowledge gaps are discussed in order to explain the motivation for this study. Thereafter an overall aim and specific objectives of the study are presented.

1.1 Background and motivation

Hg pollution poses a global threat to environmental and human health, due to its known toxicology and ability to bioaccumulate in ecosystems (Renzoni *et al.*, 1998). Human exposure to the potent toxicant methylmercury (MeHg) occurs mainly through the consumption of contaminated fish and can cause severe neurological and other defects (Ekino *et al.*, 2007; Driscoll *et al.*, 2013).

Total global Hg releases to the atmosphere are estimated at approximately 7527 $t.y^{-1}$ (Pirrone *et al.*, 2010). South Africa is currently considered to be the 6th largest Hg emitter worldwide (Pirrone *et al.*, 2010), with anthropogenic emissions estimates in the range of 27.9 – 50 $t.y^{-1}$ (Leaner *et al.*, 2009; Masekoameng *et al.*, 2010; Brunke *et al.*, 2012; Scott & Mdluli, 2012). In 2013, South Africa became a signatory of the Minamata Convention on Hg, a global treaty that aims to reduce worldwide Hg emissions (Scott & Mdluli, 2012). Since then, Hg has also been identified as a pollutant of possible national future concern (South Africa, 2018). Therefore, it is reasonable to expect that Hg might be included as a criteria pollutant in the National Ambient Air Quality Standards (NAAQS) of South Africa in the near future.

Currently, continuous atmospheric Hg measurements are conducted at limited locations in South Africa. These locations include the Cape Point Global Atmosphere Watch (CP GAW) station at the southern tip of the Cape Peninsula, operated by the South African Weather Service, as well as sites in the Vaal Triangle Air-shed and Highveld Priority Areas, which are managed by major stakeholders in the fossil fuels industry. The CP GAW station is positioned to primarily sample air masses that have passed over the southern oceanic background (Brunke *et al.*, 2012). Although the sites in the Vaal Triangle Air-shed and Highveld Priority Areas are situated in the South African interior, air masses sampled there are relatively polluted (Lourens *et al.*, 2011; Laban *et al.*, 2018). Considering all the afore-mentioned and

studies available in the peer reviewed public domain that focus on atmospheric Hg in the interior of South Africa (e.g., Venter *et al.*, 2015; Belelie *et al.*, 2019; Meyer, 2019), it is evident that measurements at background locations in the South African interior is lacking.

In order to inform and set realistic future emission and/or ambient limits/standards for Hg in the NAAQS, a better understanding of atmospheric Hg concentrations in South Africa, including interior background concentrations, is essential. This dissertation serves to partially fulfil the need for atmospheric Hg measurements at regional background sites in the South African interior.

1.2 Aim and objectives

The overall aim of this study was to measure and interpret atmospheric Hg concentrations at a regional background site in the South African interior. The specific objectives were to:

1) Conduct total gaseous mercury (TGM) measurements at a suitable background site in the South African interior for at least one seasonal cycle.
2) Calculate and contextualise the average TGM concentration at the selected site.
3) Identify and explain temporal patterns in the measured TGM dataset.
4) Identify and explain spatial patterns in the measured TGM dataset.
5) Provide insight into potential sources and/or contributing factors that influenced the TGM concentrations at the selected measurement site.

CHAPTER 2

Literature review

A literature survey on atmospheric mercury (Hg) pollution is presented in this chapter. The history of Hg and its production is explored. The atmospheric Hg cycle is discussed in detail, including the emission sources, speciation, chemical transformation pathways, and deposition of Hg. The bioaccumulation of Hg in the environment and its toxicity in humans are discussed. Lastly, legislation regarding air quality management in South Africa and its implications are briefly reviewed.

2.1 Atmospheric pollution

2.1.1 General composition and structure of the atmosphere

Earth's atmosphere consists of a mixture of several gases (Brimblecombe, 1995), which can be classified according to their quantity relative to each other (Mészáros, 1981). Gases comprising approximately 1% or more of the atmosphere (e.g., nitrogen, oxygen and argon) are classified as main constituents (Mészáros, 1981). The rest of the atmosphere is composed of trace constituents, which in turn is made up of trace gases and aerosols (Mészáros, 1981). Table 2.1 shows the chemical composition of the atmosphere and the ratios of its constituents in relation to one another.

Table 2.1: *Chemical composition of Earth's atmosphere. Adapted from Mészáros (1981) and Brimblecombe (1995).*

Constituent	Percentage
Major constituents	99.964%
Nitrogen	78.084%
Oxygen	20.946%
Argon	0.934%
Trace constituents	0.036%

According to Mészáros (1981) the chemical composition of air is regulated and maintained by atmospheric mixing in the first 80-100 km layer of the atmosphere, known as the homosphere. This lower layer of the atmosphere is followed by the heterosphere above it, of which the composition can differ due to the effects of solar radiation. The heterosphere is also called the ionosphere, due to the presence of high concentrations of free electrons and positive ions (Mészáros, 1981). The homosphere can be further divided into four vertical layers based on

thermal variations with altitude (Harrison, 1999). These layers are termed the troposphere, stratosphere, mesosphere and thermosphere (Mészáros, 1981; Brimblecombe, 1995; Seinfeld & Pandis, 2016). The atmospheric pressure across these layers is inversely related to the altitude above the earth's surface (Brimblecombe, 1995). Figure 2.1 illustrates the vertical structure of the homosphere.

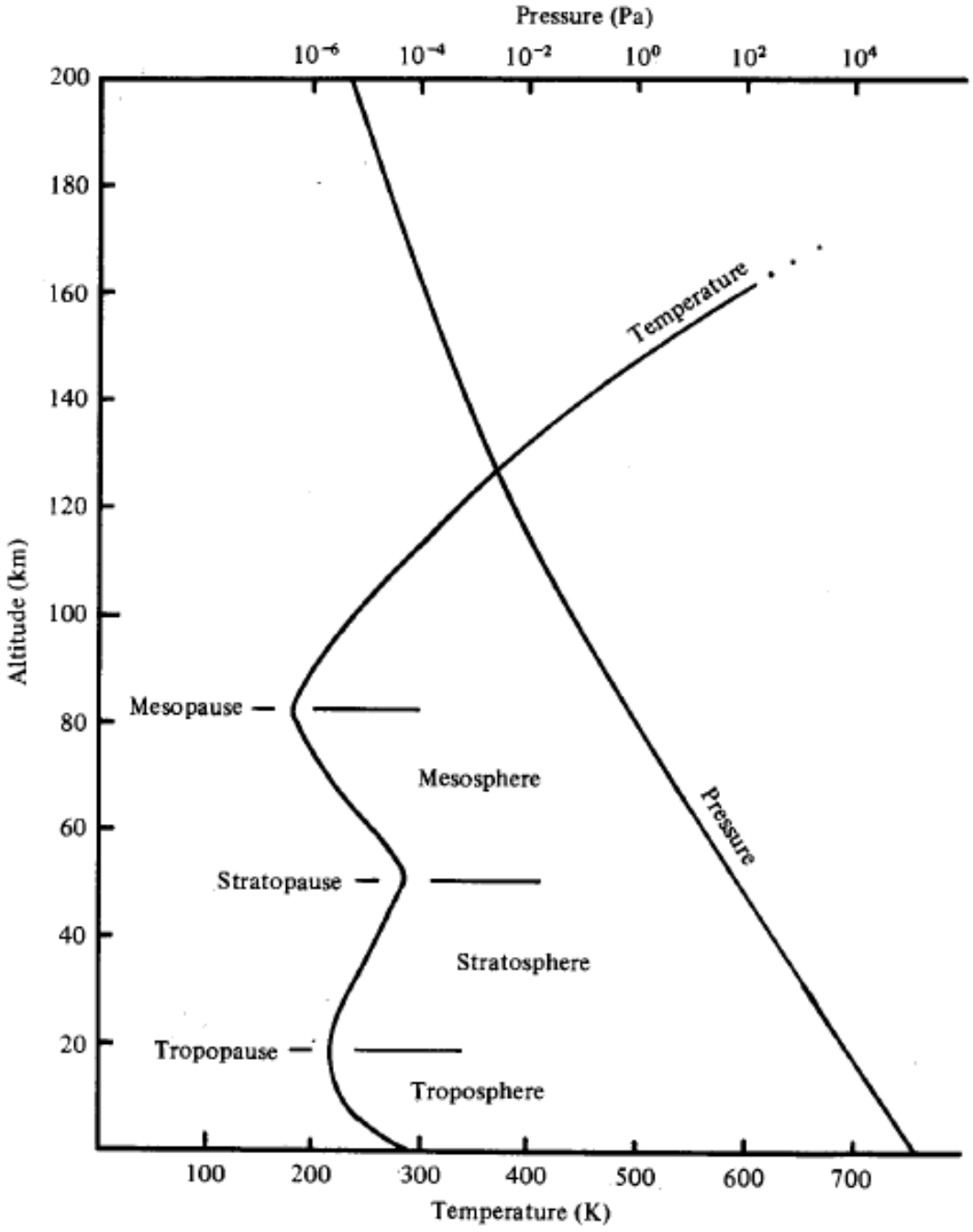

Figure 2.1: *Vertical structural profile of the homosphere, showing temperature and pressure variations with altitude. Figure provided with permission, Brimblecombe (1995). The thermosphere and heterosphere are not shown.*

As is evident from Figure 2.1, the atmospheric layer closest to earth's surface is the troposphere. In this layer life forms reside and chemical pollutants are normally emitted due to anthropogenic activities (Atkinson, 2000; Seinfeld & Pandis, 2016). In the troposphere pollutants generally have a limited lifespan, also known as atmospheric residence time, due the action of several removal processes on these pollutants, such as oxidation and deposition (Harrison, 1999). On the other hand, pollutants can also be emitted directly into the stratosphere where they will have longer residence times due to slower mixing processes (Harrison, 1999) and can be transported globally (Brimblecombe, 1995).

Atmospheric circulation is brought about by solar radiation and the earth's rotation (Brimblecombe, 1995; Harrison, 1999). This results in the transport of pollutants throughout the atmosphere (Harrison, 1999). However, where southerly and northerly air flows meet, in a region known as the intertropical convergence zone near the equator, it is difficult for air from the northern and southern hemispheres to mix (Brimblecombe, 1995). Therefore, pollutants are often present in different concentrations in the two hemispheres (Brimblecombe, 1995).

2.1.2 Categories of atmospheric pollutants

Air pollutants can be defined as any substances in the atmosphere which can cause harm to life forms, including fauna, flora and especially humans (Kampa & Castanas, 2008). There are four main categories of air pollutants: gaseous pollutants, persistent organic pollutants, heavy metals and particulate matter (Kampa & Castanas, 2008). Table 2.2 gives an overview of these categories and shows that combustion processes is one of the most prominent emission sources for the majority of air pollutants. Gaseous pollutants and particulate matter (also known as aerosols), are of special importance since they also have a pronounced effect on climate change.

Table 2.2: *Types of atmospheric pollutants. Compiled from Kampa & Castanas (2008) and Harrison (1999).*

Pollutant category	**Examples of pollutants**	**Examples of anthropogenic sources**
Gaseous pollutants	Ozone (O_3), carbon monoxide (CO), nitrogen oxides (NO_x), sulphur dioxide (SO_2), volatile organic compounds (VOCs)	Combustion of fossil fuels, road transport
Persistent organic pollutants	Pesticides, dioxins	Agriculture, combustion of plastics
Heavy metals	Lead (Pb), Mercury (Hg)	Combustion of fossil fuels, factories, waste incineration
Particulate matter	Dust, soot, smoke	Factories, power plants, waste incineration, construction activity

2.1.3 Effects of air pollution on climate change

A delicate balance between incoming and outgoing solar radiation is required in order to maintain the global average temperature on Earth (Ramanathan & Feng, 2009). Many gaseous pollutants, such as CO, methane (CH_4) and water vapour (H_2O) are classified as greenhouse gases (Connell, 2005; Seinfeld & Pandis, 2016). Greenhouse gas and aerosol emissions from anthropogenic activities, especially CO_2 emissions, have caused changes in the composition of the atmosphere, which in turn is influencing the climate system (Andreae, 2007). Greenhouse gases increase atmospheric temperature by absorbing and re-emitting infrared radiation (Ramanathan & Feng, 2009; Seinfeld & Pandis, 2016). On the other hand, aerosols can act by reflecting solar radiation away from the Earth's surface, creating a cooling effect (Andreae, 2007). Certain larger aerosols, such as soot or dust, can simultaneously warm the atmosphere by absorbing solar radiation and cool the earth's surface by reflecting radiation (Andreae, 2007). However, this effect is negligible for smaller aerosols from anthropogenic origin (Ramanathan & Feng, 2009). The cooling effect of aerosols on atmospheric temperature have the ability to mask the true extent of the warming effect caused by greenhouse gases, which is much larger (Ramanathan & Feng, 2009).

2.1.4 General health effects of air pollutants

Humans are exposed to air pollutants mainly via inhalation and ingestion through contaminated food and water sources, after which it can be absorbed through the respiratory or gastrointestinal tract (Kampa & Castanas, 2008). Air pollutants have been shown to adversely impact human health in a number of ways, which could contribute to increased hospital admissions and mortality rates (Kampa & Castanas, 2008; Kim *et al.*, 2013).

According to Kampa & Castanas (2008) the health effects of air pollutants can be classified as acute, chronic not including cancer, and cancerous. Many major systems in the human body are affected by these pollutants, including the respiratory, cardiovascular, nervous, urinary and digestive systems. Furthermore, exposure to air pollutants have been linked to an increase in the occurrence of allergic diseases and chemical sensitivities (Kim *et al.*, 2013). Foetal development can also be severely affected by maternal exposure to air pollutants, especially heavy metals (Kampa & Castanas, 2008), such as Hg.

2.2 History of Hg and its production

Mercury is the 80th element on the periodic table and is represented by the symbol Hg, based on its Latin name, *hydragyrum*, meaning silver water (Bank, 2012). Since Hg has a melting point of -38.87 °C, in its elemental form it exists as a silver liquid at room temperature (Schroeder & Munthe, 1998; Bank, 2012; Sigma-Aldrich, 2015). Elemental Hg (Hg^0) has historically been used in a wide variety of products, including thermometers, barometers, fluorescent lightbulbs and electrical switches (Bank, 2012).

Hg-bearing ores are mined from 26 Hg belts, spread across the globe (Rytuba, 2003). The most abundant Hg-containing ore is cinnabar (HgS), an example of which is depicted in Figure 2.2 (Schroeder & Munthe, 1998; Rytuba, 2003; Gray *et al.*, 2004; Stetson *et al.*, 2009; Bank, 2012). The extraction of elemental Hg from cinnabar is performed by heating the ore in a rotary, or retort furnace at 600-700ºC (Stetson *et al.*, 2009). However, this process is incomplete and results in the formation of calcined waste product, which can contain up to 25% of the original Hg found in the ore (Gray *et al.*, 2004; Stetson *et al.*, 2009). Reduced prices and a lower demand for Hg, coupled with growing environmental concerns about the release of Hg into the environment, has resulted in the decline of Hg-bearing ore mining since the 1980's (Rytuba, 2003; Gray *et al.*, 2004). Instead, the currently preferred method of Hg production, is obtaining it as a by-product when mining other ores that are enriched in Hg, such as gold (Rytuba, 2003; Bank, 2012).

Figure 2.2: *Cinnabar (red, HgS) ore containing elemental mercury (silver beads, Hg^0). (with permission, Wilson, 2020).*

2.3 The atmospheric Hg cycle

Hg is released from various sources into the atmosphere, usually into the planetary boundary layer (PBL), which is the lowest layer of the troposphere that is in contact with the earth's surface (Schroeder & Munthe, 1998). Atmospheric Hg can subsequently undergo a large variety of chemical transformations that convert Hg from one form to another (Duan *et al.*, 2017). The chemical cycling of Hg in the atmosphere is shown in Figure 2.3, in which emission sources and deposition pathways are also indicated. Hg sources, speciation, transformation and deposition are discussed in Sections 2.3.1 – 2.3.4.

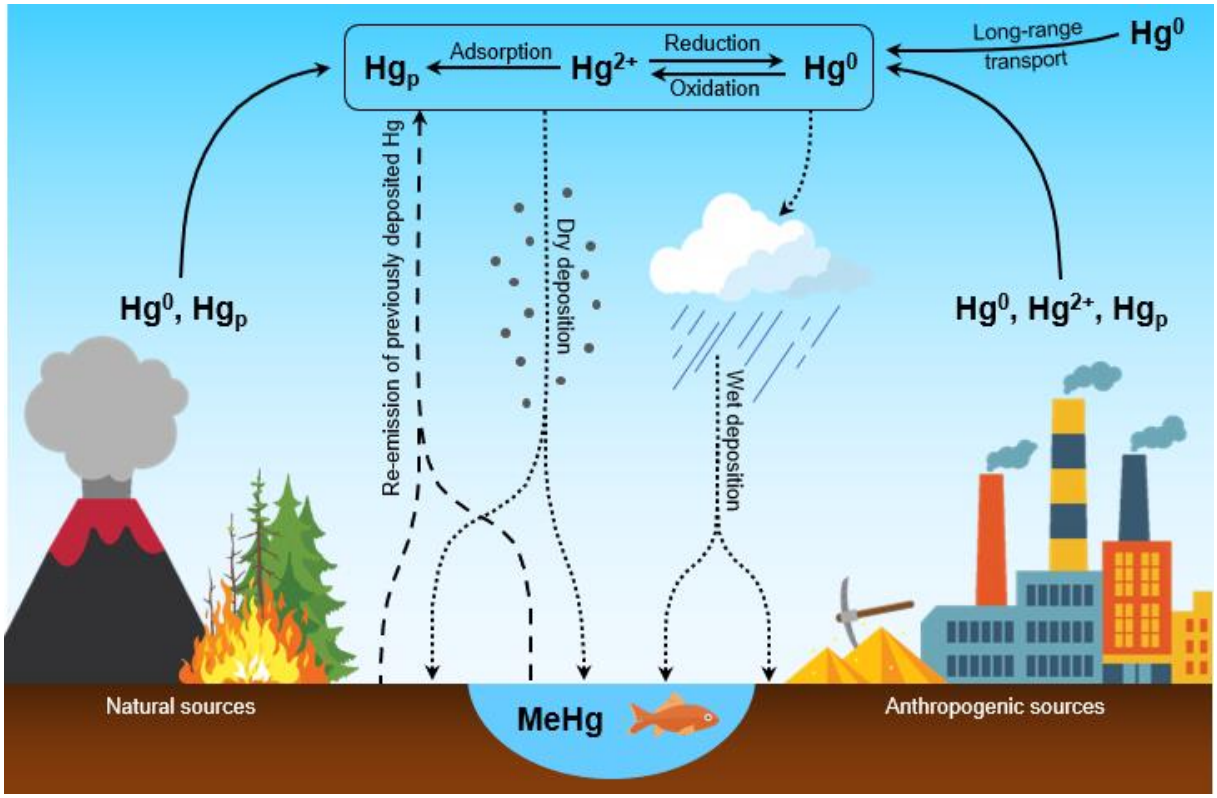

Figure 2.3: *The atmospheric Hg cycle. Solid lines indicate primary emissions, dashed lines indicate re-emissions, and dotted lines indicate deposition pathways. Adapted from Kim & Zoh (2013) and Lyman et al. (2019).*

2.3.1 Hg emission sources

Total global Hg releases to the atmosphere were calculated to amount to approximately 7527 $t.y^{-1}$ by Pirrone *et al.* (2010). Of this, the afore-mentioned authors estimated that around 2320 $t.y^{-1}$ originated from anthropogenic sources, while 5207 $t.y^{-1}$ was contributed by natural emissions, including re-emissions. The latter is significantly higher than a previous estimate of 3000 $t.y^{-1}$ by Schroeder & Munthe (1998). Future Hg emissions are projected to be in the range of 2390 – 4860 $t.y^{-1}$ in 2050, depending on the use of fossil fuels for power generation in developing countries and the implementation of associated desulphurisation technologies (Streets *et al.*, 2009). It should be emphasized that the above-mentioned values are only

estimates, since there are many uncertainties associated with current Hg emission inventories (Pacyna *et al.*, 2016).

2.3.1.1 Natural sources

Natural sources of atmospheric Hg include primary emissions from soils, water bodies, vegetation, wild fires, volcanic activity and outgassing of the earth's crust (Schroeder & Munthe, 1998; Gaffney, 2014), as well as re-emissions of previously deposited Hg, which in turn could have originated from natural or anthropogenic sources (Pirrone *et al.*, 2010). Primary natural emissions, together with re-emissions, drive background atmospheric Hg concentrations (Gaffney, 2014). Low levels of atmospheric Hg (i.e., background concentrations) have been present in the atmosphere since before recorded history. However, these levels have increased significantly after the First Industrial Revolution, as shown by measurements from peat, lake sediments and ice cores (Gaffney, 2014; Enrico *et al.*, 2017). Table 2.3 summarises global Hg emissions by natural sources for 2008. As is evident from this data, Hg emissions from surface waters (both salt- and freshwater) account for approximately 54% of natural emissions, with the remaining 46% originating from terrestrial areas (Pirrone *et al.*, 2010). Emissions from primary natural sources accounted for approximately 4% of terrestrial outputs in 2010 (Pirrone *et al.*, 2010).

Table 2.3: *Global Hg emission estimates by natural sources for 2008 (Pirrone et al., 2010).*

Source	**Hg emission estimate ($t.y^{-1}$)**	**Contribution (%)**
Oceans	2682	52
Lakes	96	2
Forests	342	7
Tundra/Grassland/Savannah/Prairie/Chaparral	448	9
Desert/Metalliferous/Non-vegetated zones	546	10
Agricultural areas	128	2
Evasion after Hg depletion events	200	4
Biomass burning	675	13
Volcanoes and geothermal areas	90	2
Total	***5207***	***100***

In South Africa, a variety of natural Hg sources possibly contribute to atmospheric Hg concentrations. As indicated by Pacyna *et al.* (2016) and as presented in Table 2.3, oceans are considered to be the largest natural contributor to atmospheric Hg concentrations. Recent findings by Bieser *et al.* (2020) support this finding, specifically in the Southern Hemisphere. These authors determined that the warm Agulhas Current to the south-east of South Africa was a significant source of elevated atmospheric Hg levels, measured at Cape Point, South Africa, between 2007 and 2016.

Open biomass burning is the second largest natural source of atmospheric Hg globally (see Table 2.3), with approximately 31% of global biomass burning events taking place in Southern Hemisphere Africa (van der Werf *et al.*, 2017). Considering this, open biomass burning ought to be a major contributor to South African atmospheric Hg concentrations. In fact, Brunke *et al.* (2001) observed a 45% increase in atmospheric Hg, relative to background concentrations, during a particularly large biomass burning event in the Cape Peninsula.

Indirect degassing of the earth's crust via the weathering of Hg containing mineral deposits such as HgS, as well as soils contaminated by Hg mine waste, could contribute to atmospheric Hg concentrations (Rytuba, 2003). Figure 2.4 below indicates the distribution of several types of Hg containing mineral deposits across South Africa, as well as the location of the Monarch Cinnabar Mine. The mine was operational between 1940 and 1946 and produced approximately 150 tonnes of metallic Hg (Cairncross & Dixon, 1995).

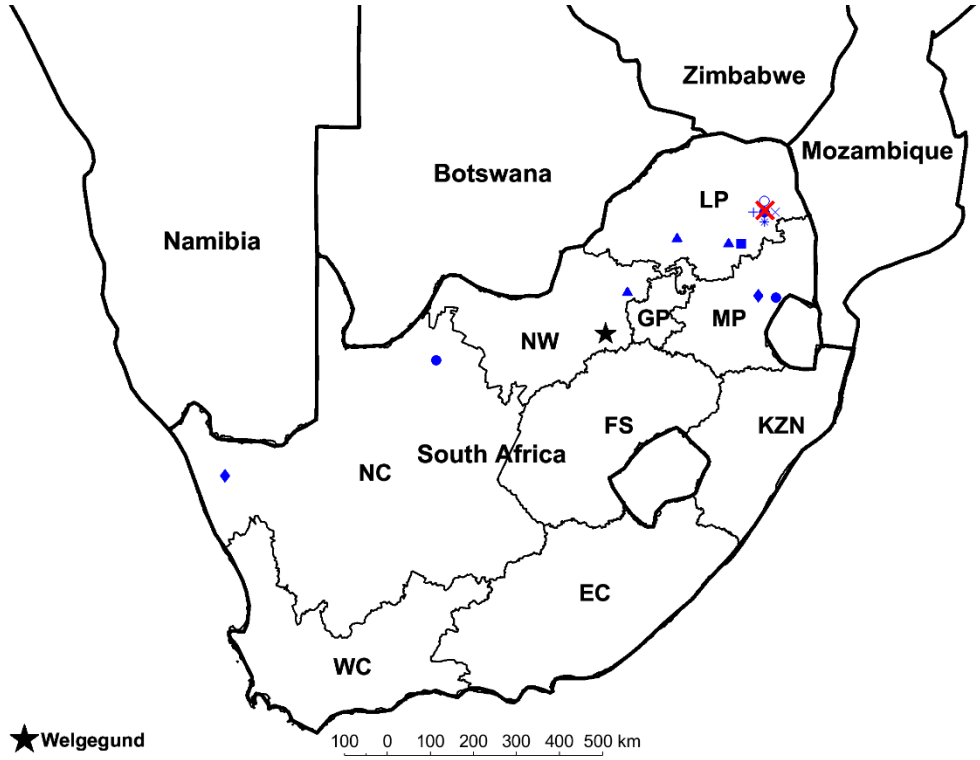

Figure 2.4: *Spatial distribution of Hg containing mineral deposits in South Africa. The red 'X' indicates the location of the Monarch Cinnabar Mine.* ■ *= Atheneite,* ● *= Cinnabar,* ♦ *= Coloradoite,* + *= Eglestonneite,* o *= Hypercinnabar,* x *= Elemental Hg,* ✳ *= Metacinnabar,* ▲*= Potarite (Mindat.org, 2020).*

2.3.1.2 Anthropogenic sources

Anthropogenic sources of atmospheric Hg include fossil fuel combustion, incineration of municipal and medical waste, sewage sludge, small-scale gold mining, ferrous and non-ferrous metals production, cement production and the chlor-alkali industry (Schroeder & Munthe, 1998; Pirrone *et al.*, 2010). Table 2.4 provides only a rough estimate of global Hg

emissions from anthropogenic sources, since emissions are constantly affected by rapid economic development, particularly in emerging countries. As is also evident from Table 2.4, the combustion of fossil fuels, especially coal, is considered to be the largest contributor to global anthropogenic Hg emissions, followed by artisanal and small-scale gold mining (Pirrone *et al.*, 2010; Street, 2015; Pacyna *et al.*, 2016; Gworek *et al.*, 2017).

Table 2.4: *Global anthropogenic Hg emissions estimates for 2010. Adapted from Pirrone et al. (2010).*

Source	**Hg emission estimate ($t.y^{-1}$)**	**Contribution (%)**
Coal and oil combustion	810	35
Non-ferrous metal production	310	13
Pig iron and steel production	43	2
Cement production	236	10
Caustic soda production	163	7
Hg production	50	2
Artisanal gold mining production	400	17
Waste disposal	187	8
Coal bed fires	32	2
VCM production	24	1
Other	65	3
Total	***2320***	***100***

Anthropogenic sources of atmospheric Hg in South Africa specifically, include commercial coal use in electricity, fuel and metal production processes; household coal combustion; cement production; crude oil refining; artisanal gold mining; waste incineration and consumer products (Leaner *et al.*, 2009; Masekoameng *et al.*, 2010; DEA, 2011; Street, 2015). South Africa has been ranked as the 2nd largest emitter of atmospheric Hg, after China, in a global anthropogenic Hg emission inventory conducted by Pacyna *et al.* (2006) in 2000. However, since then much lower revised South African emission estimates have been published, as presented in Table 2.5. As a result, South Africa is currently considered to be the 6th largest atmospheric Hg emitter worldwide (Pirrone *et al.*, 2010).

Table 2.5: *South African atmospheric Hg emission estimates from anthropogenic sources.*

Period	**TGM emission estimate ($t.y^{-1}$)**	**Reference**
2000	256.7	Pacyna *et al.* (2006)
2004	40.2	Leaner *et al.* (2009)
2006	50.0	Masekoameng *et al.* (2010)
2007 – 2009	27.9*	Brunke *et al.* (2012)

* Based on the assumption that 53% of TGM is GEM.

Figure 2.5, originally published by Masekoameng *et al.* (2010), presents annual Hg emission estimates from various anthropogenic sources in South Africa between 2000 and 2006. A

clear increase in atmospheric Hg emissions over this period can be observed. It is evident from this figure that coal-fired power plants are the largest anthropogenic source of atmospheric Hg emissions in South Africa. The country relies on 14 coal-fired power plants to generate approximately 93% of the electricity consumed (Garnham & Langerman, 2016). Hg emissions from these power plants were estimated to be between 2.6 and 17.6 $t.y^{-1}$ in 2004 (Dabrowski *et al.*, 2008), while a more recent study placed emission estimates between 16.8 and 22.6 $t.y^{-1}$ in 2015 (Garnham & Langerman, 2016). However, it is projected that Hg emissions from these power plants will be reduced by up to 13% by 2026, due to the installation of sulphur dioxide abatement technologies, which has the added benefit of decreasing Hg emissions (Garnham & Langerman, 2016).

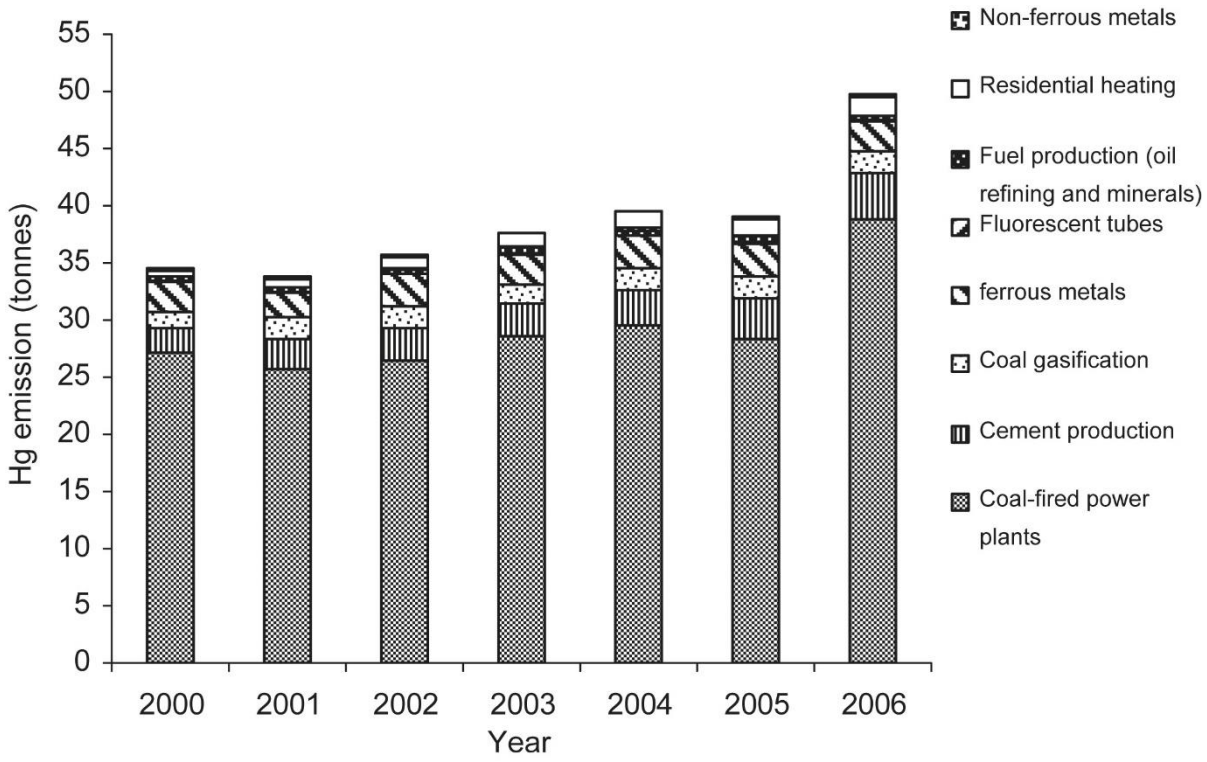

Figure 2.5: *Estimated combined atmospheric Hg emissions from various anthropogenic sources in South Africa, from 2000 – 2006 (with permission, Masekoameng et al., 2010).*

Small scale, artisanal gold mining is widespread within South Africa, despite its dangerous nature and associated health and safety risks. The process involves using elemental Hg to extract gold from ores via amalgamation (Street, 2015). The resulting amalgam is then heated to separate the Hg from the gold, releasing toxic Hg vapours (Esdaile & Chalker, 2018). In South Africa artisanal gold mining is an illegal activity, which makes it difficult to determine the extent of atmospheric Hg emissions from this sector. However, taking into account emissions from small scale gold mining in neighbouring countries, as well as the number of workers in the South African sector, it is estimated that emissions amount to less than 3 – 5 $t.y^{-1}$ (Leaner *et al.*, 2009).

2.3.2 Atmospheric Hg speciation

Hg is found in various species/forms in the atmosphere. The three forms are generally defined as gaseous elemental mercury (GEM/Hg^0), gaseous oxidised mercury (GOM/Hg^{2+}) and particulate bound mercury (PBM/Hg_p) (Gustin *et al.*, 2015; Duan *et al.*, 2017; Gworek *et al.*, 2017). These three species are collectively known as total gaseous mercury (TGM = GEM + GOM + PBM). It might also be possible for Hg to exist in the +1 oxidation state, although only in trace amounts (Schroeder & Munthe, 1998).

The speciation and concentration of atmospheric Hg is dependent on a number of factors, including: the proximity to sources, availability of oxidants, meteorology, surface conditions, and aerosol properties and concentrations (Lyman *et al.*, 2019). Hg^0 is generally thought to be the dominant species of atmospheric Hg (Lindberg & Stratton, 1998; Cole *et al.*, 2014) and is estimated to comprise roughly 95% of all atmospheric Hg (Duan *et al.*, 2017; Gworek *et al.*, 2017). However, several other studies summarized by Gustin *et al.* (2015) presented field data where Hg^{2+} was shown to comprise roughly 25% of TGM in the planetary boundary layer and 100% of TGM in the arctic during a depletion event. Hg^0 has a long atmospheric residence time compared to other metals found in the atmosphere, with estimates ranging between 6 months and 2 years (Lindqvist & Rodhe, 1985; Schroeder & Munthe, 1998; Duan *et al.*, 2017; Gworek *et al.*, 2017). This long atmospheric residence time also gives Hg^0 the ability to be transported over long distances. In contrast, the atmospheric residence times of Hg^{2+} and Hg_p are in the order of hours and days (Lindqvist & Rodhe, 1985; Gworek *et al.*, 2017), implying that these two species are quickly deposited.

2.3.3 Chemical transformation pathways

Hg is distinctly different from other metals in the atmosphere in that it is primarily found in the gaseous phase, which is relatively inert, instead of the solid phase (Lin & Pehkonen, 1997; Schroeder & Munthe, 1998). Hg^0 is readily oxidised to Hg^{2+} by the loss of its two $6s^2$ electrons (Horowitz *et al.*, 2017). These Hg^{2+} species are highly water soluble and reactive, and may occur as gases, or become associated with particles to form Hg_p (Lindberg & Stratton, 1998; Lyman *et al.*, 2019). This results in the reduced atmospheric lifespan of these species due to increased deposition rates (Horowitz *et al.*, 2017; Lyman *et al.*, 2019), as well as larger potential for accumulation in the biosphere (Meyer, 2019). Hence, it is crucial to understand the redox chemistry of Hg, as previously presented in Figure 2.3.

2.3.3.1 Gas-phase chemistry

Table 2.6 presents some of the most important oxidation reactions of Hg^0 in the gaseous phase. Until recently, ozone (O_3) and the associated hydroxyl radical ($OH^{\bullet}$) were thought to

be the major oxidants of Hg^0 in the gaseous phase (Lin & Pehkonen, 1999; Calvert & Lindberg, 2005). However, several authors have questioned this due to the relatively slow reaction rates under atmospheric conditions (Table 2.6, Calvert & Lindberg, 2005; Dibble *et al.*, 2012), as well as the thermal instability of the reaction products (Horowitz *et al.*, 2017).

Table 2.6: *Chemistry of Hg^0 oxidation in the gaseous phase.*

Oxidant	Potential reaction mechanism	Rate Constant (cm^3 $molec^{-1}$ s^{-1})	Reference
O_3	$Hg^0 + O_3 \rightarrow HgO + O$	$(3.0 \pm 2) \times 10^{-19}$	Lin & Pehkonen (1999)
$OH^\bullet$	$Hg^0 + OH^\bullet \rightarrow {}^\bullet HgOH$	3.2×10^{-3}	Pal & Ariya (2004)
	${}^\bullet HgOH + O_2 \rightarrow HgO + HO_2^\bullet$	$(9.0 \pm 1.3) \times 10^{-14}$	Pal & Ariya (2004)
H_2O_2	$Hg^0 + H_2O_2 \rightarrow Hg(OH)_2$	8.5×10^{-19}	Lin & Pehkonen (1999)
$NO_3^\bullet$	$Hg^0 + NO_3^\bullet \rightarrow HgO + NO_2$	4×10^{-15}	Sommar *et al.* (1997)
Br_2	$Hg^0 + Br_2 \rightarrow HgBr_2$	$(0.9 \pm 0.2) \times 10^{-16}$	Ariya *et al.* (2002)
Cl_2	$Hg^0 + Cl_2 \rightarrow HgCl_2$	$(2.6 \pm 0.2) \times 10^{-18}$	Ariya *et al.* (2002)
$Br^\bullet$	$Hg^0 + Br^\bullet \rightarrow HgBr^\bullet$	$(3.2 \pm 0.3) \times 10^{-12}$	Ariya *et al.* (2002)
$Cl^\bullet$	$Hg^0 + Cl^\bullet \rightarrow HgCl^\bullet$	$(1.0 \pm 0.2) \times 10^{-11}$	Ariya *et al.* (2002)

Since Holmes *et al.* (2006) suggested that gaseous phase Hg^0 oxidation is dominated by atomic bromine ($Br^\bullet$), instead of O_3 and $OH^\bullet$, many studies have contributed new insights on this hypothesis (e.g., Ariya *et al.*, 2002; Goodsite *et al.*, 2004; Ye *et al.*, 2016; Bieser *et al.*, 2017; Gencarelli *et al.*, 2017; Travnikov *et al.*, 2017). $Br^\bullet$ oxidation is widely thought to proceed via a two-step mechanism. First, photolytically-produced atomic Br oxidises Hg^0 to yield unstable $HgBr^\bullet$, which can then react with other radicals (e.g., $Br^\bullet$, $OH^\bullet$, $HO_2^\bullet$, etc.) to form inorganic Hg compounds, or dissociate back to Hg^0 (Lyman *et al.*, 2019). Potential sources of $Br^\bullet$ in South Africa include emissions from waste incineration and open biomass burning specifically in the savannah biome, as well as smouldering combustion from coal-fired power plants, coal dumps and household combustion (Meyer, 2019).

Even though the majority of recent work has focused on the oxidation of Hg^0 by O_3, $OH^\bullet$ and $Br^\bullet$, several other oxidants have also been suggested, including $Cl^\bullet$, H_2O_2 and $NO_3^\bullet$ (Lin & Pehkonen, 1999; Pacyna *et al.*, 2016; Si & Ariya, 2018; Lyman *et al.*, 2019). It has been suggested that $Br^\bullet$ oxidation plays a larger role in the Marine Boundary Layer (MBL) (Ye *et al.*, 2016), upper troposphere (Bieser *et al.*, 2017) and polar regions (Goodsite *et al.*, 2004) than in other atmospheric environments such as the continental PBL. Also, $Br^\bullet$ oxidation alone cannot explain all field observations and trends. It therefore remains possible that slower reactions with O_3 and $OH^\bullet$ dominate Hg^0 oxidation during the day at inland and coastal sites, while H_2O_2 is the dominant oxidant at night at these sites (Ye *et al.*, 2016; Si & Ariya, 2018; Lyman *et al.*, 2019). Recently it has also been shown that the rapid photoreduction of Hg^+ and Hg^{2+} species back to Hg^0 could largely offset the fast oxidation of Hg^0 by $Br^\bullet$, implying that

there are still Hg oxidation pathways in the troposphere that have not yet been identified (Saiz-Lopez *et al.*, 2020). A more complex mechanism involving multiple oxidants, of which the dominance thereof is dependent on location, time of day and time of year, is likely responsible for gaseous Hg oxidation on local, regional and global scales (Lyman *et al.*, 2019). Much uncertainty around the chemical mechanisms for Hg^0 oxidation stem from the fact that possible oxidation pathways have been determined by chemical modelling work, wherein the kinetics of the included chemical reactions are highly variable and unsure (Lyman *et al.*, 2019).

2.3.3.2 Aqueous-phase chemistry

Chemical reactions in the aqueous phase can take place on the surface of solid aerosols, or within liquid aerosols, such as cloud and fog droplets (Lyman *et al.*, 2019). Several studies have investigated the redox pathways of Hg in the aqueous phase (e.g., Munthe, 1992; Lin & Pehkonen, 1997; Wang & Pehkonen, 2004; Si & Ariya, 2008). The proposed principal redox reactions of Hg in the aqueous phase and associated rate constants are presented in Table 2.7.

Table 2.7: *Redox chemistry of Hg^0 in the aqueous phase.*

Oxidant/ Reductant	Potential reaction mechanism	Rate Constant	Reference
	Oxidation pathways		
O_3	$Hg^0 + O_3 \rightarrow Hg^{2+} + OH^- + O_2$	$(4.7 \pm 2.2) \times 10^{7}$ [a]	Munthe (1992)
$OH^\bullet$	$Hg^0 + OH^\bullet \rightarrow Hg^+ + OH^-$	2.0×10^{9} [a]	Lin & Pehkonen (1997)
	$Hg^+ + OH^\bullet \rightarrow Hg^{2+} + OH^-$	10^{10}	Lin & Pehkonen (1997)
HOCl	$Hg^0 + HOCl \rightarrow Hg^{2+} + Cl^- + OH^-$	$(2.09 \pm 0.06) \times 10^{6}$ [a]	Lin & Pehkonen (1998)
OCl^-	$Hg^0 + OCl^- \xrightarrow{H^+} Hg^{2+} + Cl^- + OH^-$	$(1.99 \pm 0.05) \times 10^{6}$ [a]	Lin & Pehkonen (1998)
HOBr	$Hg^0 + HOBr \rightarrow Hg^{2+} + Br^- + OH^-$	0.28 ± 0.02 [a]	Wang & Pehkonen (2004)
OBr^-	$Hg^0 + OBr^- \xrightarrow{H^+} Hg^{2+} + Br^- + OH^-$	0.27 ± 0.04 [a]	Wang & Pehkonen (2004)
	Reduction pathways		
SO_3^{2-}	$HgSO_3 + H_2O \rightarrow Hg^0 + \text{products}$	0.0106 ± 0.0009 [b]	Van Loon *et al.* (2000)
$HO_2^\bullet$	$Hg^{2+} + HO_2^\bullet \rightarrow Hg^+ + O_2 + H^+$	1.7×10^{4} [a]	Pehkonen & Lin (1998)
	$Hg^+ + HO_2^\bullet \rightarrow Hg^0 + O_2 + H^+$		Pehkonen & Lin (1998)
$R(COO)_2^{2-}$	$Hg^{2+} + R(COO)_2^{2-} \rightarrow Hg(OOC)_2R$	$(1.2 \pm 0.2) \times 10^{4}$ [a,c]	Si & Ariya (2008)
		$(4.9 \pm 0.8) \times 10^{3}$ [a,d]	Si & Ariya (2008)
		$(2.8 \pm 0.5) \times 10^{3}$ [a,e]	Si & Ariya (2008)
hv	$Hg(OH)_2 \xrightarrow{hv} Hg^0 + \text{products}$	3×10^{-7} [b]	Nriagu (1994)

(a) Unit = $M^{-1}\ s^{-1}$
(b) Unit = s^{-1}
(c) Oxalic acid, R = None
(d) Malonic acid, R = CH_2
(e) Succinic acid, R = $(CH_2)_2$

The reduction of Hg^{2+} to Hg^0 has not been as widely studied as Hg oxidation pathways, but models have suggested that Hg^{2+} reduction in the atmosphere takes place mainly through aqueous phase photo-reduction (Saiz-Lopez *et al.*, 2018). Hg reduction pathways include the reduction of Hg^{2+} by sulphite (SO_3^{2-}), photo-reduction of Hg^{2+} by the hydroperoxyl radical ($HO_2^{\bullet}$), photo-reduction of Hg^{2+}-dicarboxylic acid complexes, and photoreduction of mercury(II) hydroxide ($Hg(OH)_2$) (Si & Ariya, 2018). Hg^{2+} reduction in the atmosphere competes with deposition pathways, thus influencing deposition patterns (Saiz-Lopez *et al.*, 2018).

2.3.4 Deposition

Atmospheric deposition is the predominant pathway through which Hg is removed from the atmosphere and injected into terrestrial and aquatic environments. Deposition can proceed via wet and dry mechanisms (Figure 2.3; Schroeder & Munthe, 1998). Dry deposition occurs when Hg compounds fall to the earth's surface under gravity and are taken up by soil, water or vegetation (Zannetti, 1990; Beckett *et al.*, 1998; Jiskra, *et al.*, 2018). Wet deposition involves the absorption of Hg^{2+} and Hg_p into droplets, followed by precipitation (e.g., rain or snow) or impaction (e.g., dew formation and fog droplets) to the earth's surface (Zannetti, 1990; Harrison, 1999; Barber *et al.*, 2004).

The removal of Hg^0 from the atmosphere via deposition proceeds slowly due to its very low water solubility (Lindberg *et al.*, 2007), implicating Hg^{2+} as the main candidate for atmospheric deposition. In fact, Hg^{2+} has been shown to have dry deposition velocities and scavenging ratios more than an order of magnitude higher than Hg^0 (Lindberg & Stratton, 1998; Lindberg *et al.*, 2002). Understanding the phase partitioning of Hg^{2+} is important since it greatly influences the deposition thereof (Seinfeld & Pandis, 2016). As previously mentioned, Hg^{2+} can react with other atmospheric species to form gases, or associate with particles in the atmosphere to form Hg_p (Section 2.3.3). The main drivers of this gas-particle partitioning are air temperature, the chemical composition of aerosols and the presence of an aerosol aqueous phase (Lyman *et al.*, 2019). Due to the low volatility of Hg^{2+} compounds, they partition to the gaseous phase at higher temperatures, but shift to the particle phase at lower temperatures (Lin & Pehkonen, 1999; Lyman *et al.*, 2019). This was also shown in a modelling study by Amos *et al.* (2012) where models suggested that approximately 90% of Hg^{2+} existed in the gas phase in warm air, compared to only around 10% in cold air. An experimental study by Rutter & Schauer (2007) confirmed that the gas-particle partitioning of Hg^{2+} is highly dependent on aerosol composition. The authors showed that Hg^{2+} readily partitioned to and remained in the particle phase if NaCl is considered as the aerosol, while Holmes *et al.* (2009) described the uptake of Hg^{2+} by aqueous sea salt aerosols. This has significant implications

for Hg^{2+} removal by sea salt aerosols in coastal and marine environments and implicates sea salt as a sink for Hg (Selin *et al.*, 2007).

2.4 Hg bioaccumulation and toxicity

Hg deposited on terrestrial surfaces is mostly retained by soils and vegetation, but can also enter waterbodies through leaching, runoff and erosion processes (Kocman *et al.*, 2013). Here, inorganic Hg species can be converted to organic methylmercury (MeHg, Figure 2.3) in water or sediments, mostly via anaerobic microbial activity (Tang *et al.*, 2020), or undergo photo-reduction to dissolved gaseous mercury (DGM) in water (Luo *et al.*, 2020). The bioaccumulation of MeHg along the food chain is of great concern, since it is highly toxic to both animal species and humans (Renzoni *et al.*, 1998).

The primary route of human exposure to MeHg is through the ingestion of contaminated food, mainly fish and shellfish (Driscoll *et al.*, 2013). However, MeHg formation has also been shown to occur in rice paddies and subsequently accumulates in rice (Feng *et al.*, 2008; Meng *et al.*, 2018). This is extremely concerning since fish constitutes at least 15% of the per capita intake of animal protein for 3 billion people around the world (Driscoll *et al.*, 2013), while rice is a dietary staple for about half of the global population (Zhao *et al.*, 2020). Other routes of Hg exposure include inhalation, emissions from dental amalgam fillings, and vaccines containing the preservative thimerosal (Bjørklund *et al.*, 2017).

Once Hg is introduced into the body it is readily transported. What makes it such a dangerous toxicant is its ability to easily pass through cell membranes, allowing it to cross the blood-brain barrier and the placenta (Andreoli & Sprovieri, 2017). Therefore, the most vulnerable groups with regards to Hg toxicity are the developing foetus, pregnant women and women of child-bearing age, due to its negative impact on fertility, foetal development and pregnancy outcome (Driscoll *et al.*, 2013; Bjørklund *et al.*, 2019). The most well-known case of large-scale MeHg poisoning occurred in Minamata Bay, Japan, in 1953, through the consumption of contaminated fish and shellfish (Ekino *et al.*, 2007). This incident raised awareness of the severe neurological disease that can develop as a result of MeHg poisoning, which was subsequently termed Minamata Disease. Symptoms of MeHg poisoning include visual and hearing impairment, loss of muscle coordination, somatosensory disturbances and psychiatric disorders (Ekino *et al.*, 2007).

The negative impacts of Hg on the environment and especially humans prompted the United Nations Environment Programme (UNEP) to become actively involved in bridging the gap between the science of Hg poisoning and policy implementation since 2001 (UNEP, 2017). Their efforts ultimately resulted in the development of the Minamata Convention on Mercury

(naming derived from the above-mentioned incident in Minamata Bay, Japan), a global legally binding treaty that focusses on protecting the environment and human health from anthropogenic releases of Hg and Hg compounds (*Minamata Convention on Mercury,* 2013). Since the treaty was adopted in 2013 and came into effect in 2016, it has been signed by 128 countries, including South Africa.

2.5 Air quality management in South Africa

South Africa has been plagued by relatively poor ambient air quality in some areas since the 1960's, mainly due to pollution from industrial "hotspots", such as the Vaal Triangle (Naiker *et al.*, 2012). This led to the introduction of the Atmospheric Pollution Prevention Act (APPA) in 1965 which focussed mainly on controlling industrial emissions, but it was later considered ineffective in dealing with air pollution (Naiker *et al.*, 2012). Ultimately, the APPA was replaced by the National Environmental Management: Air Quality Act (AQA) in 2005, as an updated approach to combatting ambient air pollution in South Africa (South Africa, 2005; Naiker *et al.*, 2012). Since then, numerous notices and regulations regarding air quality management have been published in the Government Gazette of South Africa, including the introduction of National Ambient Air Quality Standards (NAAQS) (South Africa, 2009), as well as the declaration of three national priority areas for air quality management (South Africa, 2005, 2007, 2012) which are shown in Figure 2.6.

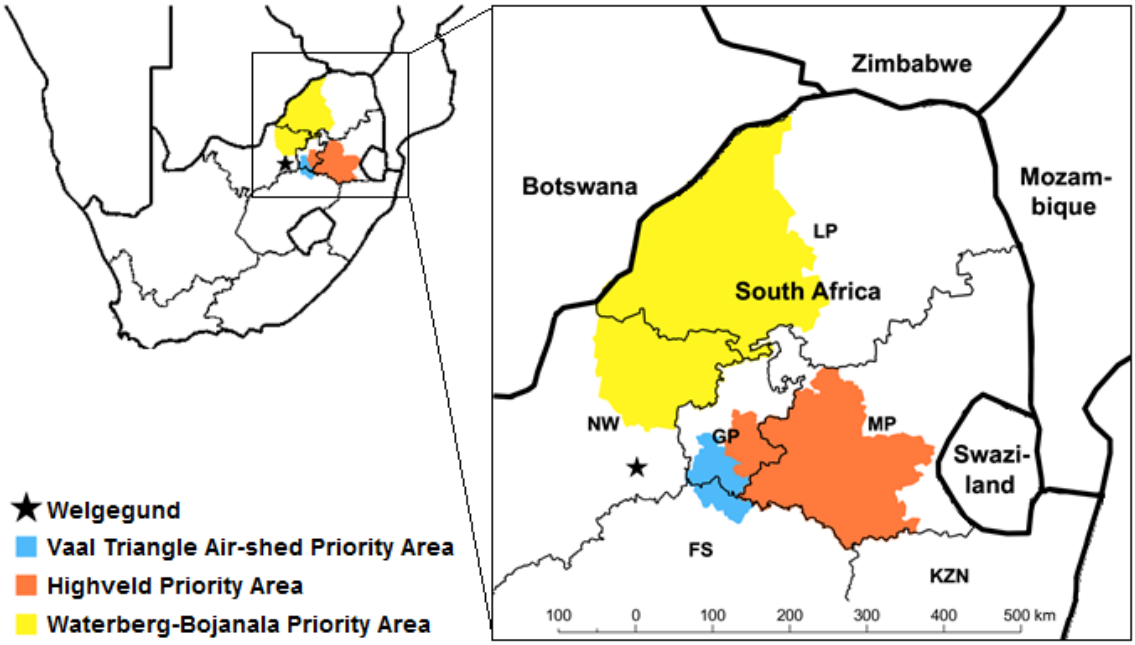

Figure 2.6: *National priority areas for air quality management in South Africa. Map compiled using area boundaries published in the Government Gazette of South Africa.*

South Africa has taken four major steps towards reducing atmospheric Hg pollution. Firstly, the South African Mercury Assesment (SAMA) Programme was establshed in 2007 to develop

a framework for Hg research in South Africa, through collaboration between academia, government and non-governmental organisations (Leaner, 2007). Secondly, although the NAAQS do not currently include emission limits for Hg, the 2017 National Framework for Air Quality Management has identified Hg as a pollutant of possible future concern on a national scale (South Africa, 2018). Therefore, it is reasonable to expect that emission and/or ambient limits/standards for Hg might be introduced into the NAAQS in the near future. Thirdly, as previously mentioned (Section 2.4), South Africa has been a signatory of the Minamata Convention on Mercury since its inception in 2013. The ratification of the treaty in 2019 has far reaching implications for the country. Scott & Mdluli (2012) proposed that South Africa would have to focus on reducing the production and use of Hg containing products (e.g., medical devices), implement measures to reduce Hg emissions from major anthropogenic sources (e.g., coal-fired power plants), identify areas that contribute to Hg contamination (e.g., historic gold tailings dumps) and obtain financial and technical support in order to successfully achieve the objectives of the treaty. Lastly, the Department of Science and Innovation has recently funded the establishment of the South African Mercury Network (SAMnet) (Mbatha & Martin, 2020). This is a Hg monitoring network of five proposed ambient monitoring sites, five wet deposition sites and numerous passive sampling sites across the country. The locations of the proposed SAMnet ambient Hg monitoring sites are shown in Figure 2.7.

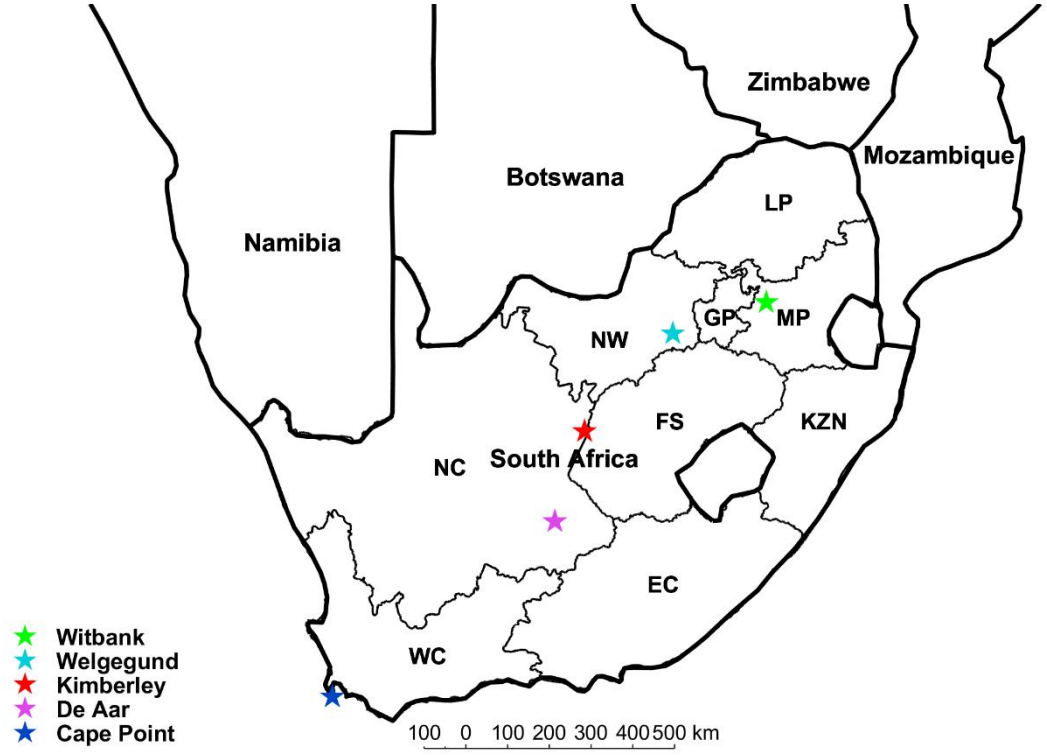

Figure 2.7: *Locations of proposed SAMnet ambient Hg monitoring sites. Province abbreviations: WC – Western Cape, NC – Northern Cape, EC – Eastern Cape, FS – Free State, NW – North West, GP – Gauteng Province, LP – Limpopo Province, MP – Mpumalanga Province, KZN – KwaZulu-Natal.*

CHAPTER 3

Experimental

This chapter explains the experimental procedures that were followed. Detailed descriptions of the measurement site, instrumentation used to conduct total gaseous mercury (TGM) measurements and data processing steps are provided. Instrumentation used to obtain auxiliary data are also briefly discussed.

3.1 Site description

The Welgegund atmospheric measurement station (hereafter only referred to as Welgegund) depicted in Figure 3.1, is situated roughly 25 km north-west of Potchefstroom, South Africa (26°34'10"S, 26°56'21"E, 1480 m.a.s.l.). Temperatures in the area typically range between minimums of 0°C in winter and maximums of 30°C in summer (Venter *et al.*, 2020). Precipitation over the area varies greatly across seasons, with the wet season spanning from approximately middle October to April and almost no precipitation occurring during the rest of the year (Venter *et al.*, 2020).

The measurement station is located on a commercial cattle and crop (mainly maize and some sunflower) farm. Vegetation in the area consists mostly of grasses, as well as some perennials and herbs (Mucina & Rutherford, 2006; Jaars *et al.*, 2016). The soil in the area consists primarily of sandy silt, which is formed mainly via rock weathering (Jaars *et al.*, 2016).

The geology underlying the measurement site and the immediate area is comprised mainly of quartzite and shale rocks belonging to the Witwatersrand supergroup, interspersed with a variety of igneous and sedimentary formations, e.g., volcanic, basalt and shale rocks from the Ventersdorp supergroup (Council for Geoscience, 2019). There are no large Hg containing rock formations within approximately 100 km of Welgegund (see Figure 2.4 and associated text) that could potentially contribute to atmospheric Hg concentrations.

Although local pollution sources surrounding the site are minimal, polluted air masses from the Johannesburg-Pretoria megacity, the Waterberg Priority Area, the Vaal Triangle Air-shed Priority Area and the Highveld Priority Area (South Africa, 2005, 2007, 2012) frequently pass over the site. However, clean air injections from the sparsely populated western parts of South Africa offset these polluted plumes.

Figure 3.1: *Welgegund during the winter season.*

3.2 Materials and methods

3.2.1 TGM measurement setup

TGM concentrations at Welgegund were measured using an automated Tekran® (Model 2537B) ambient Hg vapour analyser, provided by SASOL. This model did not have the capability to perform Hg speciation. The analyser was installed inside a temperature-controlled trailer with an average indoor temperature of approximately 23 °C. The analyser was connected to an inlet on top of the trailer roof via a Polytetrafluoroethylene (PTFE) sample line of approximately 5 m in length. Since the measurement campaign spanned over the warmer spring, summer and autumn months and only 1 m of the sample line was located outside the trailer, it was decided not to insulate or heat the sample line. It is also important to note that the sampled air did not come into contact with any metal surfaces that could adsorb Hg prior to reaching the analyser. Hg concentrations were measured at 5 min intervals with a sample flow rate of 1.5 L/min to obtain a total sample volume of 7.5 L. These settings result in a detection limit of 0.1 ng.m^3. The carrier gas necessary for instrument operation was supplied via a pressurised argon cylinder (> 99.999 % purity supplied by Afrox (Pty) Ltd).

The analyser was calibrated automatically every 24 h using an internal permeation source. A calibration cycle comprises three steps for each gold trap: clean, zero and span. During cleaning, desorption of the gold cartridge takes place to remove any residual Hg. The zero step provides an indication of Hg contamination within the instrument, as well as the carrier gas. Zero-air required for the calibrations was produced by passing indoor ambient air through a Tekran® zero-air filter connected to the zero-air inlet on the analyser. The span operation tests the sensitivity of the instrument.

3.2.2 Operating principles of the TGM instrument

The basic operating principles of the Tekran® 2537B ambient Hg vapour analyser is described in its user manual and follows three basic steps: adsorption, desorption and detection. The overall flow through the analyser is shown in Figure 3.2 below.

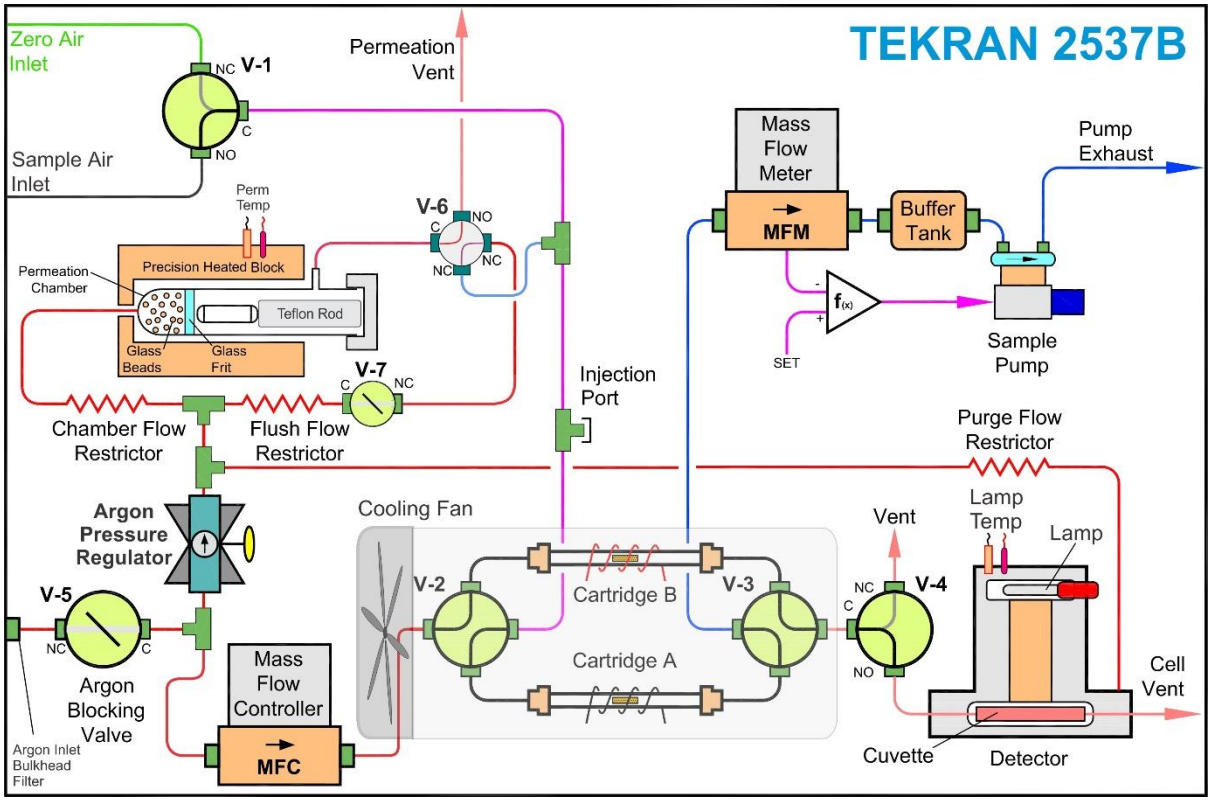

Figure 3.2: *Overall flow diagram of the Tekran® 2537B ambient Hg vapour analyser. Figure provided with permission by Tekran®.*

Firstly, sample air is passed through a 0.2 µm PTFE filter at the sample air inlet to remove particulate matter that could potentially damage the analyser. The sample then reaches one of two gold cartridges where Hg is adsorbed onto the surface of the gold cartridge. Interfering species are able to pass through the gold cartridge since the adsorption properties of gold are highly specific to Hg. While Hg is being adsorbed onto one gold cartridge during sampling, the

other gold cartridge is being desorbed. Alternating between the cartridges allows continuous sampling of the inlet stream to take place.

During desorption, the gold cartridge is heated by a surrounding heating coil. This results in the release of previously adsorbed Hg, which is carried by inert argon gas into a quartz cuvette located inside the detector cell. Hg detection is performed by cold vapour atomic fluorescence spectroscopy (CVAFS) inside the detector cell. The cuvette is irradiated at 253.7 nm by a low-pressure Hg vapour lamp, which excites any Hg atoms present within the sample. The Hg atoms subsequently fluoresce and re-emit radiation at the same wavelength, which in turn is observed by a photomultiplier tube. The intensity of the fluorescence is directly proportional to the amount of Hg in the sample. The gold cartridge and detector cell are then both flushed with argon to prepare it for the next measurement and to minimise the possibility of sample carry over.

3.2.3 TGM instrument maintenance

As stated previously (Section 3.2.1), automated internal calibrations were performed daily. Site visits to Welgegund was conducted on a weekly basis to ensure that the instrument was fully operational according to a predetermined checklist. The carrier gas cylinder, as well as the zero and sample air inlet filters, were replaced on a monthly basis. At the occurrence of more serious instrument failures (e.g., a faulty sample pump), troubleshooting and repairs were performed by the designated Tekran® service provider in South Africa.

3.3 TGM data processing

3.3.1 Quality control and statistical analyses

The raw calibration and sample data for each 24 h period was stored in a text file by the analyser. An excerpt from a typical text file can be found in Annexure A. The complete dataset that was obtained after performing the data cleaning steps described in this section is available on request from the candidate, or the study leaders.

The dataset that was collected over the measurement period at Welgegund contained 21 103 individual measurements. The entire dataset was evaluated using a fit for purpose MATLAB® script. The basic operation of this script follows: If a successful calibration was performed on any given date, all the data for that day was extracted from the corresponding text file into a matrix. Once all the data had been loaded into the matrix, the criteria in Table 3.1 was applied to each measurement to determine whether it was valid. If the measurement was invalid due to instrumental parameters being out of range, it was removed from the dataset. Fit for purpose

MATLAB® scripts were also used to do most other data processing and to generate result figures/tables.

Table 3.1: *Criteria for data removal based on general instrument parameters. Adapted from D'Amore et al. (2015).*

Description	Removal criteria
Questionable sample volume	$\lvert(Volume_{measured} - Volume_{expected})\rvert > 7\%$
Baseline voltage too low	Baseline voltage < 0.01 V
Baseline deviation too high	Baseline deviation > 0.2 V
Below detection limit	Hg concentration < 0.1 $ng \cdot m^{-3}$

3.4 Auxiliary data

Air mass histories prior to sampling at Welgegund were determined using the Hybrid Single Particle Lagrangian Integrated Trajectory (HYSPLIT) Model (version 4.820), developed by the National Oceanic and Atmospheric Administration (NOAA) Air Resources Laboratory (Draxler & Hess, 1997; Stein *et al.*, 2015; van der Werf *et al.*, 2017). Meteorological input data for the model was obtained from the Global Data Assimilation System (GDAS) archive (GDAS, 2019). 96-hour back trajectories were calculated, arriving hourly at Welgegund at a height of 100 m. Thus, 24 back trajectories were generated for each day, amounting to a total of 5736 trajectories over the sampling period.

The accuracy of a single trajectory is highly dependent on the quality of the meteorological input data, and a calculation error of around 20% of the travel distance is typical (Stohl, 1998). Therefore, overlay back trajectory maps, previously described by Venter *et al.* (2012), were used to analyse regional patterns in air mass movement and identify main fetch regions, instead of single trajectories. These maps indicate the trajectory overpass percentage for 0.2° x 0.2° grid cells, with red and blue representing the highest and lowest overpass rates respectively. Furthermore, another technique introduced by Vakkari *et al.* (2011), was employed to associate back trajectories with measured TGM and ozone (O_3) concentrations. To achieve this, a 0.5° x 0.5° grid was defined over a map of southern Africa. The hourly TGM/O_3 mean was calculated for all trajectories that had passed over each grid cell, and a corresponding colour was assigned to the cell. A minimum of 50 and 40 trajectories had to have passed over any given cell for TGM and O_3, respectively, in order for the results to have been considered statistically reliable.

Many other species/parameters are measured at Welgegund (Beukes *et al.*, 2015). However, only a limited number of additional ancillary species/parameters were considered in this study. These included O_3 concentration, relative humidity (RH) and planetary boundary layer (PBL) height. The instruments used to conduct these measurements and very brief summaries of

their operating principles are presented in Table 3.2. Maintenance checks on all instruments were conducted on a weekly and/or montly basis, and typically included flow adjustments, inlet cleaning and filter changes. This auxillary data was also quality checked and cleaned as previously described by Beukes *et al.* (2015).

Table 3.2: *Auxiliary data measured at Welgegund*

Measured property/species	**Analytical instrument**	**Operating principle**
Ozone (O_3)	Environment SA 41M O_3 analyser	Absorption of ultraviolet light by O_3
Relative humidity (RH)	Rotronic MP 101A humidity/temperature probe	Capacitive humidity sensor
Planetary boundary layer (PBL) height	Vaisala CT25K ceilometer	Light detection and ranging (LIDAR) technology, with data processing according to Gierens *et al.* (2019).

Open biomass burning events across southern Africa were determined at 500 m resolution with the Moderate Resolution Imaging Spectroradiometer (MODIS) Collection 5 burned area product (Roy *et al.*, 2008). These 500 m x 500 m pixels were superimposed on a map of southern African biomes to showcase the extent of open biomass burning and its potential impact on atmospheric Hg concentrations in South Africa.

CHAPTER 4

Results and discussion

This chapter presents the total gaseous mercury (TGM) data collected at Welgegund and contextualises it within a global setting. Temporal, including diurnal and seasonal, as well as spatial patterns in TGM concentrations are explored. The driving factors for these patterns are also discussed.

4.1 Data availability

TGM measurements were taken at Welgegund between 17 September 2016 and 5 May 2017, according to the procedure described in Section 3.2.1. The raw 5 min data was processed as described in Section 3.3.1, using the Global Mercury Observation System (GMOS) data cleaning criteria (D'Amore *et al.*, 2015) as guidelines. As previously stated, the complete dataset after data cleaning, is available on request from the candidate, or the study leaders.

Figure 4.1 shows the post data cleaning ambient TGM concentration timeseries graphically. Data availability was 30.53% after data cleaning. As is evident from the afore-mentioned figure, the low data availability was due to several large and some smaller data gaps. At the start of the measurement campaign several adjustments were made to the instrument settings, accounting for smaller data gaps in September 2016. However, the larger data gaps between October 2016 and November 2016, as well as January 2017 to March 2017, were caused by critical instrument failures which required technical repairs by the service provider of Tekran® instruments in South Africa. There were two main factors contributing to the extent of the large data gaps. Firstly, the specific TGM analyser used during this study was on loan from SASOL. The analyser was not operational for quite some time prior to being installed at Welgegund. Although initial indications were that the analyser was in good condition, it soon became apparent that this was not the case. Secondly, since the instrument was not owned by the North West University (NWU), SASOL had to approve and pay for repairs, instead of the NWU, which resulted in additional time delays. Both these factors were outside the control of the candidate. Furthermore, the measurement campaign could not be continued after May 2017, due to financial limitations associated with the project.

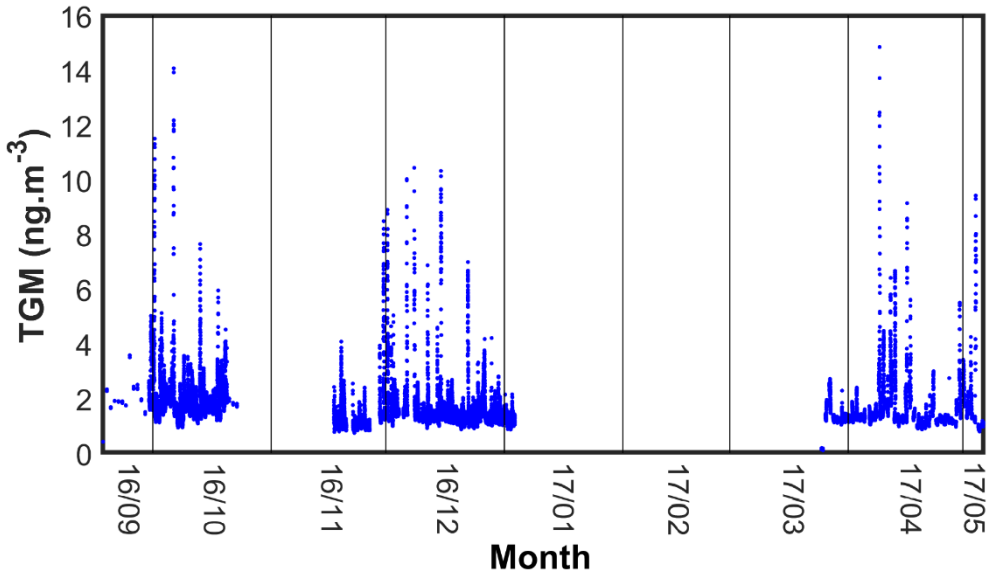

Figure 4.1: *TGM concentration vs. time, as measured at Welgegund between 27 September 2016 and 5 May 2017.*

4.2 Contextualisation of TGM concentrations

Notwithstanding the relatively small TGM dataset (as indicated in Section 4.1), the data still have significant value, considering the limited number of TGM, or gaseous elemental mercury (GEM) studies that have been published in the peer reviewed public domain for the South African interior. As far as the candidate could assess, only Belelie *et al.* (2019) published TGM data for the South African interior, with many TGM or GEM papers originating from the coastal Cape Point Global Atmosphere Watch (CPT GAW) station (e.g., Baker *et al.*, 2002; Ebinghaus *et al.*, 2010; Venter *et al.*, 2015; Bieser *et al.*, 2020; Slemr *et al.*, 2020). Measured GEM concentrations are typically slightly lower than TGM, since GEM measurements do not include Hg^{2+} or particulate bound Hg (Hg_p) concentrations. However, as described in Section 2.3.2, the difference in these measurements is almost negligible, since the majority of TGM is GEM (Lindberg & Stratton, 1998; Cole *et al.*, 2014).

The 5th, 25th, 50th (median), 75th, and 95th percentiles, as well as the minimum, mean and maximum TGM concentrations for the Welgegund measurement campaign are presented in Table 4.1. As is evident from this data, the mean value (1.68 ng.m^{-3}) is approximately 3 times closer to the 75th percentile (1.82 ng.m^{-3}) than the 25th percentile (1.24 ng.m^{-3}). This indicates that the TGM concentrations at Welgegund was more significantly influenced by plumes with higher TGM concentrations, than by relatively stable and low concentrations.

Table 4.1: *The 5th, 25th, 50th (median), 75th, and 95th percentiles, as well as the minimum, mean and maximum TGM concentrations for the Welgegund measurement campaign.*

	TGM concentration ($ng.m^{-3}$)
Minimum value	0.10
5th percentile	0.99
25th percentile	1.24
50th percentile (median)	1.43
Mean	1.68 ± 0.94 (std)
75th percentile	1.82
95th percentile	2.99
Maximum value	14.85

In order to contextualise the data presented in Table 4.1, the mean TGM concentration measured at Welgegund was compared to TGM and/or GEM mean values that were obtained elsewhere, as presented in Table 4.2. As previously stated, the difference between TGM and GEM concentrations are typically almost negligible (Lindberg & Stratton, 1998; Cole *et al.*, 2014).

The Welgegund TGM mean (1.68 $ng.m^{-3}$) was compared with data from other measurement campaigns in South Africa and correlated well with TGM data for Marapong (1.61 $ng.m^{-3}$) in the Waterberg Priority Area (Meyer, 2019), as well as with TGM concentrations at Balfour (1.99 $ng.m^{-3}$) and Standerton (1.25 $ng.m^{-3}$), both situated within the Highveld Priority Area (HPA) of South Africa (Belelie *et al.*, 2019). The TGM mean measured at Middelburg (1.04 $ng.m^{-3}$) in the HPA (Belelie *et al.*, 2019) was significantly lower than that of the afore-mentioned Balfour and Standerton values (Belelie *et al.*, 2019), even though the site is located in an area which is considered to be relatively polluted (Lourens *et al.*, 2011; Laban *et al.*, 2018). However, very little TGM/GEM data have been published for the HPA. TGM means measured at Elandsfontein (2.49 $ng.m^{-3}$) in the HPA and Sasolburg (3.95 $ng.m^{-3}$) in the Vaal Triangle Air-shed Priority Area, which are both located in close proximity to several large potential Hg point sources (Meyer, 2019), were respectively 1.5 and 2.4 times higher than the Welgegund TGM mean. The afore-mentioned priority areas were briefly introduced in Section 2.5. Furthermore, the TGM mean of Welgegund was approximately 1.5 times higher than the mean GEM reported by Venter *et al.* (2015) for Cape Point (1.09 $ng.m^{-3}$), which closely resembles Southern Hemisphere background concentrations. Annual mean TGM/GEM for the Southern Hemisphere has been reported to be in the range of 0.85 – 1.05 $ng.m^{-3}$ (Slemr *et al.*, 2015).

Measurements at two rural sites in the tropics, i.e., Kodaikanal (1.53 $ng.m^{-3}$) in India (Karthik *et al.*, 2017) and Nieuw Nickerie (1.40 $ng.m^{-3}$) in Suriname, South America (Müller *et al.*, 2012),

also resembles the Welgegund TGM mean. According to the afore-mentioned authors, TGM concentrations at both these tropical sites were influenced by local, or nearby pollution events.

When compared to TGM/GEM concentrations in the Northern Hemisphere, for which a mean/median range of 1.5 – 1.7 ng.m^{-3} has been reported (Sprovieri *et al.*, 2016), the Welgegund TGM mean is similar to means reported for rural sites such as Harwell (1.45 ng.m^{-3}) in England (Kentisbeer *et al.*, 2015) and St. Anicet (1.65 ng.m^{-3}) in Canada (Poissant *et al.*, 2005), as well as urban sites such as Helsinki (1.54 ng.m^{-3}) in Finland (Kyllonen *et al.*, 2014), Houston (1.64 ng.m^{-3}) and Reno (2.00 ng.m^{-3}) in the USA (Lyman & Gustin, 2009; Griggs *et al.*, 2020) and Minamata (1.90 ng.m^{-3}) in Japan (Marumoto *et al.*, 2015). However, it is approximately 2 to 2.6 times lower than mean concentrations reported for Asian megacities such as Seoul (3.44 ng.m^{-3}) in South Korea (Choi *et al.*, 2009), as well as Lanzhou (4.48 ng.m^{-3}) and Shanghai (4.19 ng.m^{-3}) in China (Duan *et al.*, 2017; Yin *et al.*, 2020).

The mean TGM/GEM at true background sites such as Alert (1.00 ng.m^{-3}) in Canada, which is the northernmost permanently inhabited place in the world (Cobbett *et al.*, 2007), Amsterdam Island (1.03 ng.m^{-3}) in the southern Indian Ocean (Angot *et al.*, 2014), Bariloche (0.86 ng.m^{-3}) in Argentina's Patagonia region (Diéguez *et al.*, 2019), as well as Dumont d'Urville (0.87 ng.m^{-3}) and Troll Station (0.93 ng.m^{-3}) in Antarctica (Pfaffhuber *et al.*, 2012; Angot *et al.*, 2016), were all approximately two times lower than the Welgegund TGM mean.

Table 4.2: *Hg concentrations observed at various locations across the globe, in order of decreasing latitude.*

	Location	Site Type	TGM/GEM (ng.m^{-3})	Monitoring period	Reference
Northern Hemisphere	Alert, Canada	Coastal	1.00 ± 0.40	Feb 2005 – Jun 2005	Cobbett *et al.* (2007)
	Helsinki, Finland	Urban	1.54 ± 0.20	Sep 2006 – Aug 2007	Kyllonen *et al.* (2014)
	Harwell, England	Rural	1.45 ± 0.24	Nov 2012 – Dec 2013	Kentisbeer *et al.* (2015)
	St. Anicet, Canada	Rural	1.65 ± 0.42	Jan 2003 – Dec 2003	Poissant *et al.* (2005)
	La Seyne-sur-Mer, France	Coastal	2.16 ± 0.60	Jan 2012 – Dec 2012	Marusczak *et al.* (2016)
	Reno, U.S.A.	Urban	2.00 ± 0.70	Feb 2007 – Jan 2009	Lyman & Gustin (2009)
	Seoul, South Korea	Urban	3.44 ± 2.13	Feb 2005 – Dec 2006	Choi *et al.* (2009)
	Lanzhou, China	Urban	4.48 ± 2.32	Oct 2016 – Oct 2017	Yin *et al.* (2020)
	Fukuoka, Japan	Urban	2.33 ± 0.49	Jun 2012 – May 2013	Marumoto *et al.* (2015)
	Minamata, Japan	Coastal	1.90 ± 0.40	Jun 2012 – May 2013	Marumoto *et al.* (2015)
	Shanghai, China	Urban	4.19 ± 9.13	Jun 2014 – Dec 2014	Duan *et al.* (2017)
	Houston, U.S.A.	Urban	1.64 ± 0.27	Mar 2012 – Jun 2013	Griggs *et al.* (2020)
Tropics	Celestun, Mexico	Coastal	1.05 ± 0.27	Jan 2012 – Oct 2012	Velasco *et al.* (2016)
	Calhau, Cape Verde	Coastal	1.19 ± 0.13	Dec 2011 – Dec 2015	Read *et al.* (2017)
	Kodaikanal, India	Rural	1.53 ± 0.25	Nov 2012 – Sep 2013	Karthik *et al.* (2017)
	Gunn Point, Australia	Rural	0.95 ± 0.12	Jun 2014 – Jun 2016	Howard *et al.* (2017)
	Nieuw Nickerie, Suriname	Rural	1.40 ± 0.25	Mar 2007 – Oct 2007	Müller *et al.* (2012)

Table 4.2 (continued): *Hg concentrations observed at various locations across the globe, in order of decreasing latitude.*

Southern Hemisphere	Middelburg, South Africa	Rural	1.04 ± 0.62	Jan 2009 – Dec 2009	Belelie *et al.* (2019)
	Welgegund, South Africa	**Rural**	**1.68 ± 0.94**	**Sep 2016 – May 2017**	**Present study**
	Sasolburg, South Africa	Urban	3.95 ± 2.97	Apr 2013 – Jun 2013	Meyer (2019)
	Elandsfontein, South Africa	Rural	2.49 ± 2.06	Jan 2010 – Apr 2015	Meyer (2019)
	Balfour, South Africa	Rural	1.99 ± 0.94	Jan 2009 – Dec 2009	Belelie *et al.* (2019)
	Marapong, South Africa	Rural	1.61 ± 1.42	Feb 2010 – Aug 2013	Meyer (2019)
	Standerton, South Africa	Rural	1.25 ± 1.38	Jan 2009 – Dec 2009	Belelie *et al.* (2019)
	Cape Point, South Africa	Coastal	1.09 ± 0.15*	Mar 2007 – Dec 2011	Venter *et al.* (2015)
	Amsterdam Island, French Southern and Antarctic Lands	Coastal	1.03 ± 0.08	Jan 2012 – Dec 2013	Angot *et al.* (2014)
	Bariloche, Argentina	Rural	0.86 ± 0.16	Oct 2012 – Jul 2017	Diéguez *et al.* (2019)
	Dumont d'Urville, Antarctica	Coastal	0.87 ± 0.23	Jan 2012 – May 2015	Angot *et al.* (2016)
	Troll Station, Antarctica	Coastal	0.93 ± 0.19	Feb 2007 – Jun 2011	Pfaffhuber *et al.* (2012)

* Although Cape Point is a coastal station, this value is representative of continental atmospheric Hg concentrations, determined through back trajectory analysis.

4.3 Temporal patterns

4.3.1 Diurnal

The overall average TGM diurnal cycle, as well as the three average diurnal cycles for the considered seasons (spring, summer and autumn) are presented in Figure 4.2a. As is evident, these diurnal cycles exhibited similar patterns. This is likely due to the diurnal cycle being influenced by the same factors, which are discussed further on in this section, year-round. To simplify the discussion here, only the overall average TGM diurnal cycle is explored. During the night, up to approximately 08:00 local time, the TGM concentrations were relatively stable (approx. 1.6 – 1.8 ng.m^{-3}) and similar to the average TGM concentration reported over the entire sampling period (i.e., 1.68 ng.m^{-3}). At around 08:00 the TGM concentration increased significantly and peaked between 10:00 and 11:00. The average TGM concentration observed during this peak time was approximately 2.3 ng.m^{-3}. The TGM concentration then rapidly decreased until it reached a minimum of about 1.3 ng.m^{-3} at around 17:00. From this point onwards the TGM concentration continued to rise until reaching relatively stable levels again just before midnight.

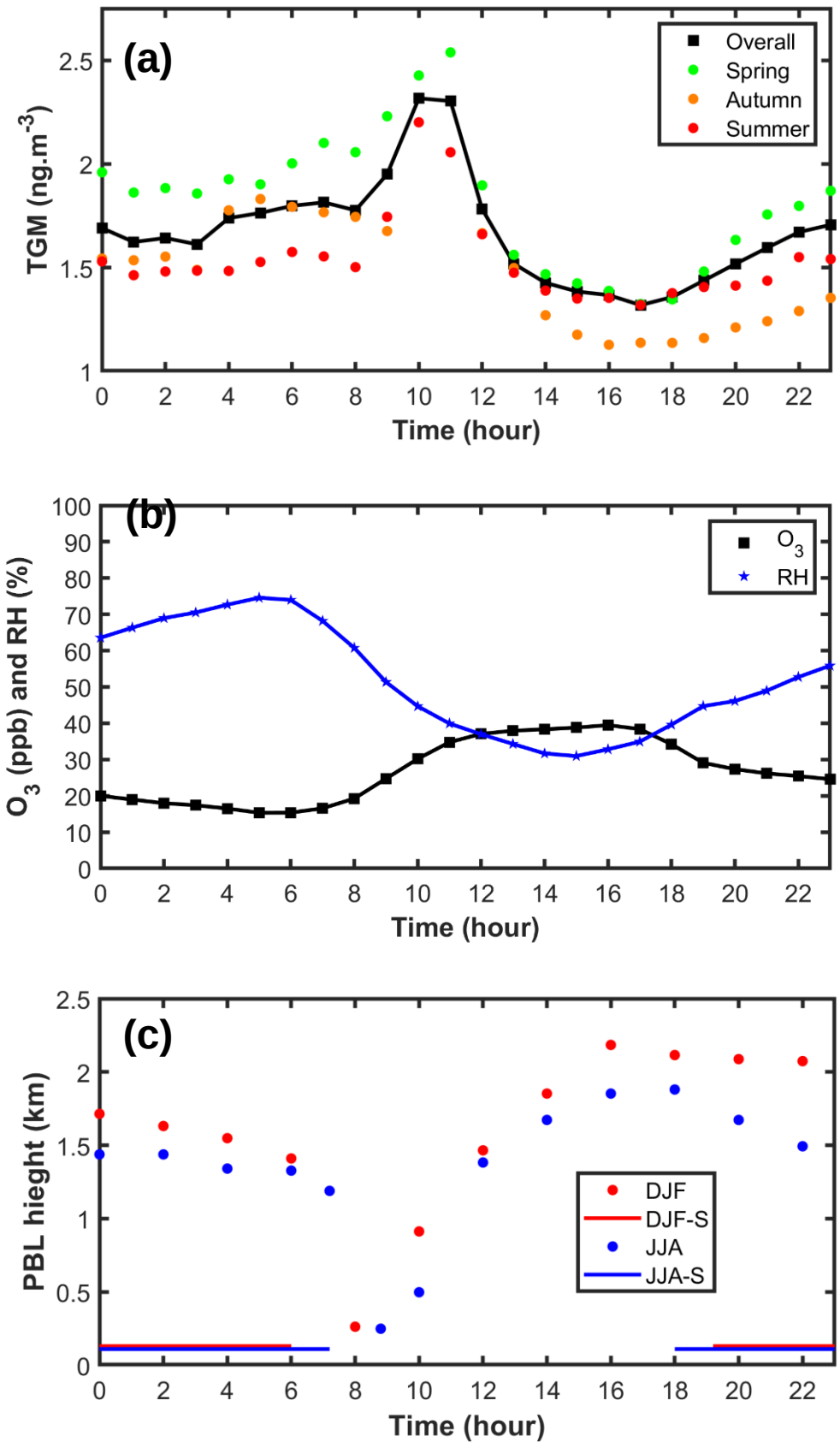

Figure 4.2: *(a) Average diurnal trends of TGM concentration, (b) O_3 concentration and RH, (c) PBL structure for summer (DJF) and winter (JJA) between October 2012 and August 2014, adapted from Gierens et al. (2019) and Venter et al. (2020).*

The most prominent feature of the TGM diurnal trend (Figure 4.2a) is the single peak that is observed during late morning. In order to understand and explain this observation, the corresponding average diurnal cycles of ozone (O_3), relative humidity (RH) and planetary boundary layer (PBL) height are presented (Figures 4.2b and c) and discussed. As can be seen by comparing Figures 4.2a and b, the trends of TGM and O_3 concentrations are roughly inverse to one another, except during the time when the TGM concentration peaked. This inverse relationship between TGM and O_3, is due to O_3 being one of the most important oxidants of Hg^0 (Horowitz *et al.*, 2017), implying that TGM will in general decrease if O_3 increases. At Welgegund O_3 concentrations reached a minimum before sunrise, after which it continued to increase and peaked 1–3 hours after maximum solar intensity. O_3 levels then steadily decreased throughout the night, until it again reached the morning minimum. A previous long-term study at Welgegund have reported a similar O_3 diurnal cycle for the South African interior (Laban *et al.*, 2018), which was ascribed to the daytime photochemical formation of O_3 from nitrogen dioxide (NO_2) in the troposphere (Seinfeld & Pandis, 2016; Laban *et al.*, 2018). Tropospheric O_3 can only form from NO_2, while O_3 precursors such as volatile organic compounds (VOCs) and carbon monoxide (CO) are sources of peroxy-radicals ($HO_2^\bullet$ and $RO_2^\bullet$) that oxidise nitrogen oxide (NO) to NO_2 (Seinfeld & Pandis, 2016).

In addition to the TGM-O_3 interaction, there was also an approximate inverse relationship observed between and O_3 and RH, as is evident in Figure 4.2b. Similar relationships have been reported specifically for the South African interior (Laban *et al.*, 2018; Meyer, 2019) and elsewhere (Jia & Xu, 2014; Meyer, 2019). This inverse relationship exists due to the photolytic breakdown of O_3 to form molecular oxygen (O_2) and atomic oxygen (O). The O then reacts with water vapour in the atmosphere (of which RH is a good indicator) to produce the very reactive hydroxyl radical ($OH^\bullet$) (Gardoni *et al.*, 2012). The $OH^\bullet$ can also oxidise Hg^0 to Hg^{2+} (Lin & Pehkonen, 1997; Seigneur *et al.*, 2006; Si & Ariya, 2018), resulting in increased deposition of Hg species and subsequently lower levels of TGM (Section 2.3.3).

The above-mentioned atmospheric chemistry involving TGM, O_3 and RH explain the overall diurnal cycle profile, but not the peak observed between 10:00 and 11:00 (Figure 4.2a). This peak is rather explained by the evolution of the PBL. The PBL over Welgegund, including the diurnal cycle and seasonal trends, was discussed in detail by Gierens *et al*. (2009). Figure 4.2c shows the typical diurnal profile of the PBL over Welgegund, measured between October 2012 and August 2014. Of specific interest is the occurrence of a low-level thermal inversion layer at approximately 100–150m depth within the PBL, which typically occurs from just after sunset to early morning. This inversion prevents mixing of layers above and below it. If the source of the TGM peak was relatively local, low-level emissions, the concentration of TGM would have peaked when the thermal inversion was intact. However, the TGM peaked after

the breakdown of the low-level inversion layer, which allowed downward mixing of air masses above the inversion. This indicates that sources further away from Welgegund, for which the TGM were transported within the PBL, but above the low-level inversion, is the most likely source of the additional TGM observed during the peak.

4.3.2 Seasonal

The monthly average TGM concentrations over the measurement period are presented in Figure 4.3, as well as the number of 5 min TGM data points available for each month. Notwithstanding the relatively low data availability discussed in Section 4.1, enough data was available in all the months, except February 2017, to give a relatively good indication of the seasonality of TGM measured at Welgegund. According to a six-year study by Venter *et al*. (2020), the dry season at Welgegund typically spans from May to middle October, with the wet season covering the rest of the year. Rain events measured at Welgegund during the specific monitoring period considered in this study are shown in Figure 4.4. From this data it is evident that the 2015/2016 dry season ended approximately in middle October 2016, and that the 2016/2017 dry season commenced after middle April 2017.

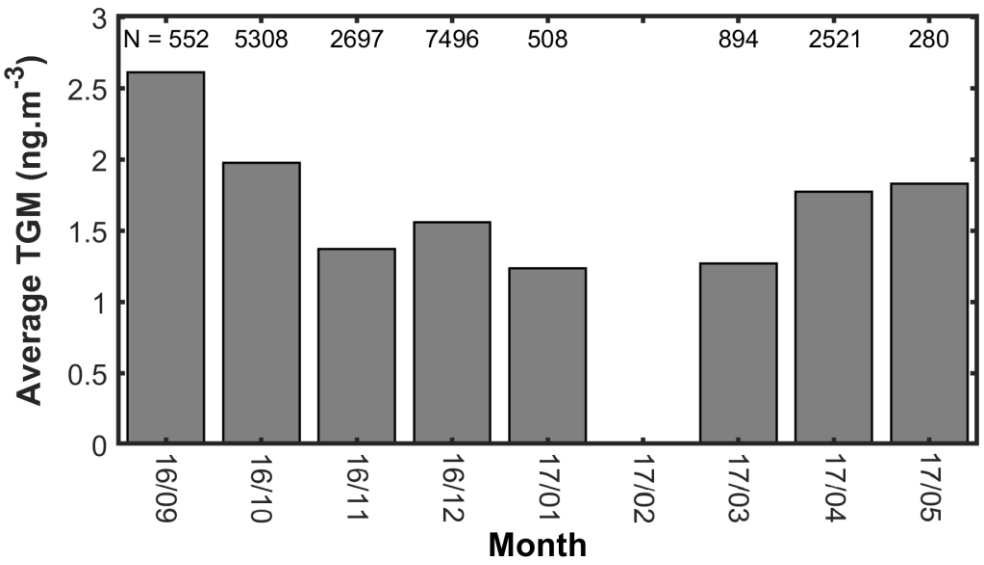

Figure 4.3: *Monthly average TGM concentrations and number of 5 min TGM data points for each month, measured at Welgegund during the measurement period.*

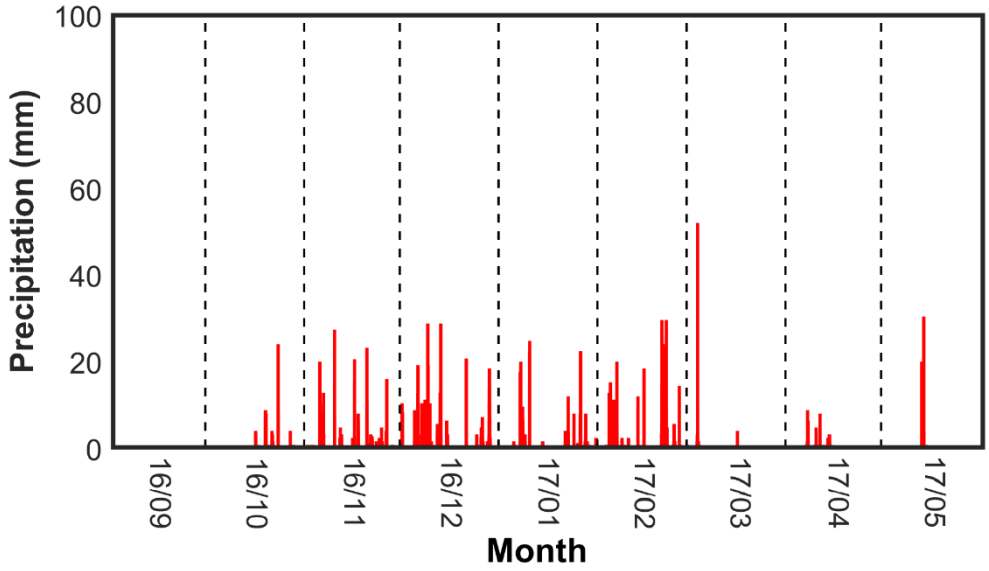

Figure 4.4: *Rain events recorded at Welgegund during the measurement period.*

By comparing Figures 4.3 and 4.4 it is clear that there is an interrelation between the wet and dry seasons, and TGM concentrations. In general, higher TGM concentrations were reported in the months associated with the dry season, and lower concentrations in the wet season. This can be expected, since increased precipitation during the wet season facilitates removal of TGM from the troposphere via wet deposition pathways (Lyman *et al.*, 2019), while emissions from open biomass burning contribute to higher levels of TGM in the troposphere during the dry season. Open biomass burning is the largest natural terrestrial source of TGM (Pirrone *et al.*, 2010). However, open biomass burning in southern Africa can be both natural and/or anthropogenic (Vakkari *et al.*, 2014; van der Werf *et al.*, 2017; Vakkari *et al.*, 2018). Differences in annual rainfall, mainly due to the variation in El Niño Southern Oscillation (ENSO) conditions, also affect the seasonality and spatial distribution of open biomass burning. La Niña results in above average rainfall, while El Niño typically causes less than average rainfall in southern Africa. This results in more, or less biomass being available, respectively, for open biomass burning in a specific year (Archibald *et al.*, 2009; Maritz *et al.*, 2020). Therefore, to contextualise the possible contribution of open biomass burning to measured TGM at Welgegund, Figure 4.5 shows the locations of open biomass burning events (MODIS collection 5 burned area product, Roy *et al.*, 2008; Section 3.4) that occurred during the period when TGM data was available (Section 4.1). These events were superimposed on a vegetation biome distribution map of southern Africa (Mucina & Rutherford, 2006).

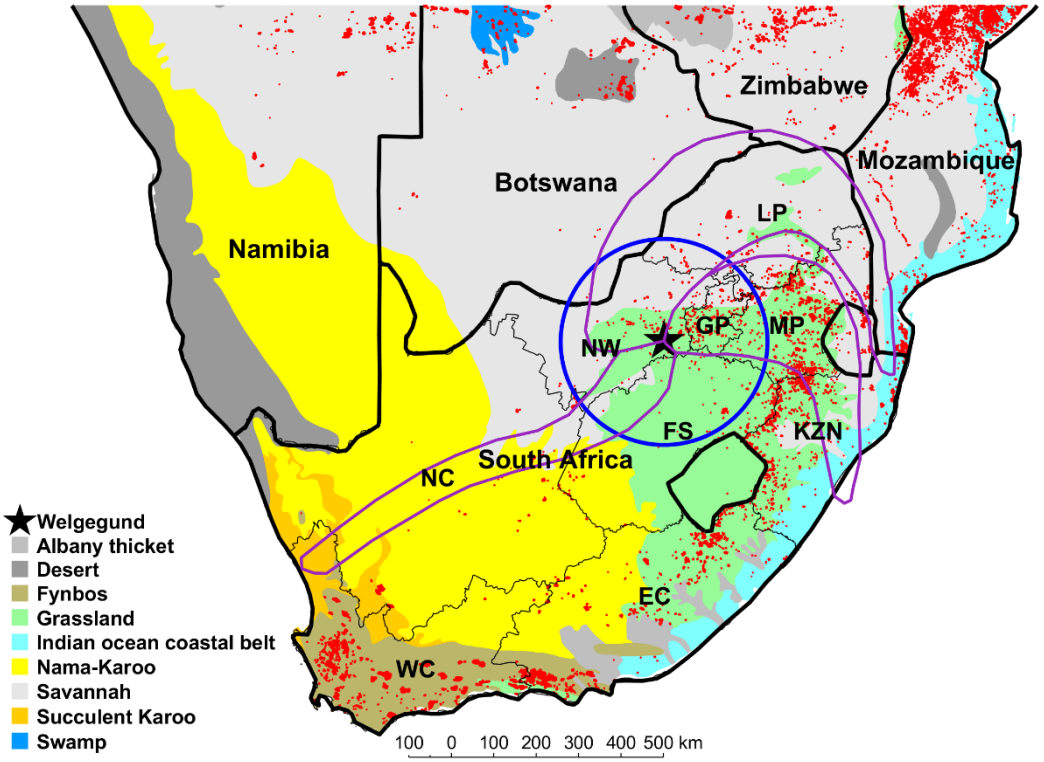

Figure 4.5: *Biome distribution map of southern Africa indicating the location of fires (red areas) that occurred during the measurement period. Adapted from (Mucina & Rutherford, 2006) and Venter et al. (2020). The blue circle represents a radius of 250 km around Welgegund, while the purple polygons indicate the three main routes, or fetch regions (see Figure 4.7 and associated text).* *Province abbreviations: WC – Western Cape, NC – Northern Cape, EC – Eastern Cape, FS – Free State, NW – North West, GP – Gauteng Province, LP – Limpopo Province, MP – Mpumalanga Province, KZN – KwaZulu-Natal.*

It is important to note that the peak open biomass burning period of the Grassland and Savannah biomes in the South African interior, which are the only two biomes found within a 250 km radius of Welgegund (see the blue circle in Figure 4.5), typically spans from late local winter to early spring (Chiloane *et al.*, 2017; Booyens *et al.*, 2019; Maritz *et al.*, 2020). Biomass burning around Welgegund specifically was investigated over a six-year period by Venter *et* al., (2020). The afore-mentioned study reported the peak open biomass burning period to be between May and mid-October. Figure 4.6 presents the monthly frequency of MODIS fire pixels within the above-mentioned 250 km radius around Welgegund. This figure clearly indicates that more open biomass burning occurred during the dry season, which also suggests that open biomass burning events in relatively close proximity to Welgegund likely resulted in the higher TGM concentrations observed during the dry season (Figure 4.3).

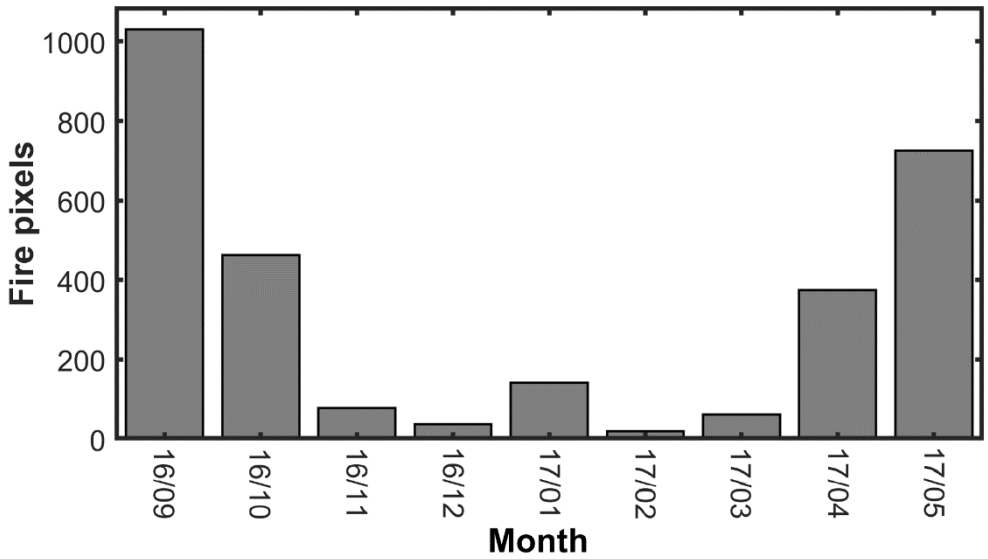

Figure 4.6: *Monthly fire counts (MODIS fire pixels) within a 250 km radius of Welgegund during the measurement period.*

4.4 Spatial patterns

Although TGM measurements were only conducted at one site, i.e., Welgegund, air mass history analysis can be used to give insight into possible sources and/or source regions that affected the measurements. Welgegund is ideally situated as a regional background site since it is not too near to large point sources and areas of very high population densities, as was illustrated in Section 3.1. This will be demonstrated later on in this section as well. Numerous authors have also previously used air mass history analyses to indicate possible sources and/or source regions for pollutant concentrations measured at Welgegund (e.g., Venter et al., 2016; Laban et al., 2018; Venter et al., 2018; Booyens et al., 2019; Venter et al., 2020).

Figure 4.7 presents an overlay back trajectory map, (introduced in Vakkari et al., 2011; Section 3.4), for 96-hour backward trajectories over the entire measurement period (17 September 2016 to 5 May 2017), but only for the times when TGM measurements were available (Section 4.1). From this map it is evident that air masses passing over Welgegund during these times followed three main routes, or fetch regions, which are indicated with polygons. The 1st route followed an anticyclonic recirculation pattern, which has previously been described for the South African Highveld in general (Tyson *et al.*, 1996) and for Welgegund specifically (Jaars *et al.*, 2014). The fetch region of this route was over the northern parts of the South African interior, mostly just south east, south and south west of the respective borders with Botswana, Zimbabwe and Mozambique. The 2nd fetch region was mostly almost directly east of Welgegund, covering the Johannesburg-Pretoria megacity and the Mpumalanga Highveld before stretching across parts of KwaZulu-Natal. The fetch region of the 3rd route was south west of Welgegund and included areas of mostly lower population

densities. The 1st fetch region had significantly higher overpass frequencies (dark red areas in Figure 4.7), if compared to the other two regions.

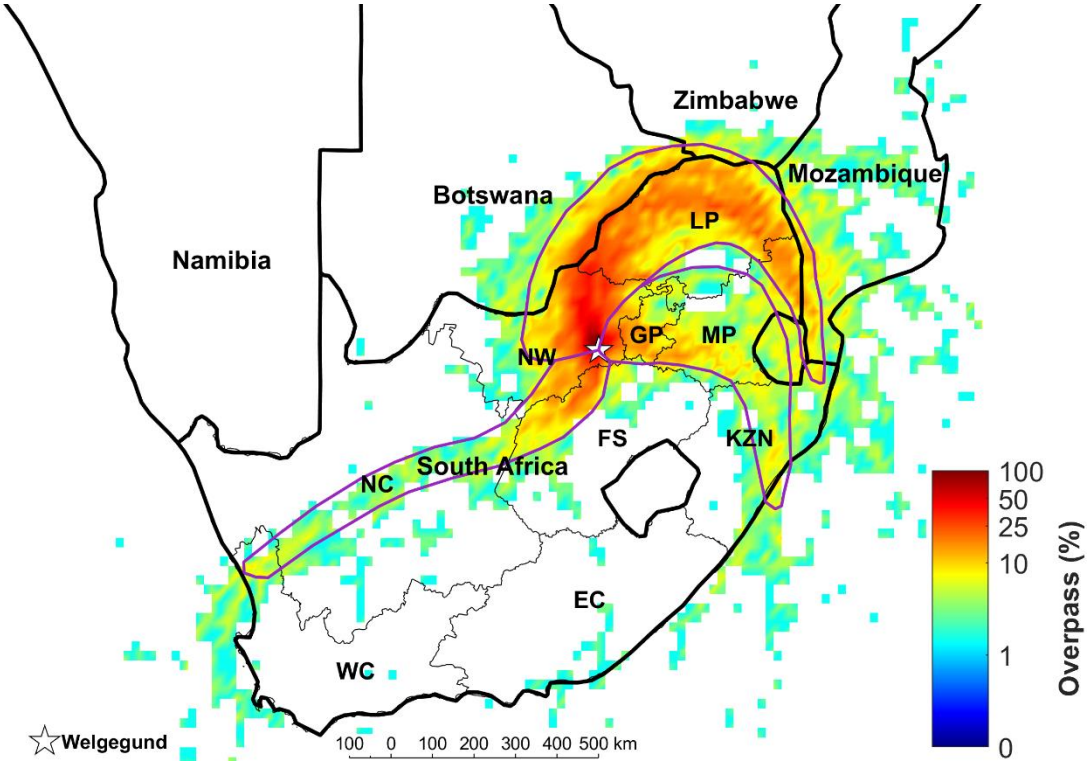

Figure 4.7: *Overlay back-trajectory map of air masses sampled at Welgegund for the period that TGM data were available. The polygons indicate the three main routes, or fetch regions. Province abbreviations: WC – Western Cape, NC – Northern Cape, EC – Eastern Cape, FS – Free State, NW – North West, GP – Gauteng Province, LP – Limpopo Province, MP – Mpumalanga Province, KZN – KwaZulu-Natal.*

To understand and/or interpret the importance of the above-mentioned air mass histories, it must be contextualised within aspects such as higher population densities, locations of large potential point sources, as well as biomes and the occurrence of open biomass burning – all factors that could possibly contribute to increased TGM concentrations. The population density across southern Africa and the locations of major point sources in the interior of South Africa are shown in Figure 4.8. Both these aspects serve as indicators of anthropogenic activities, which is important within the context of TGM emissions (Pirrone *et al.*, 2010).

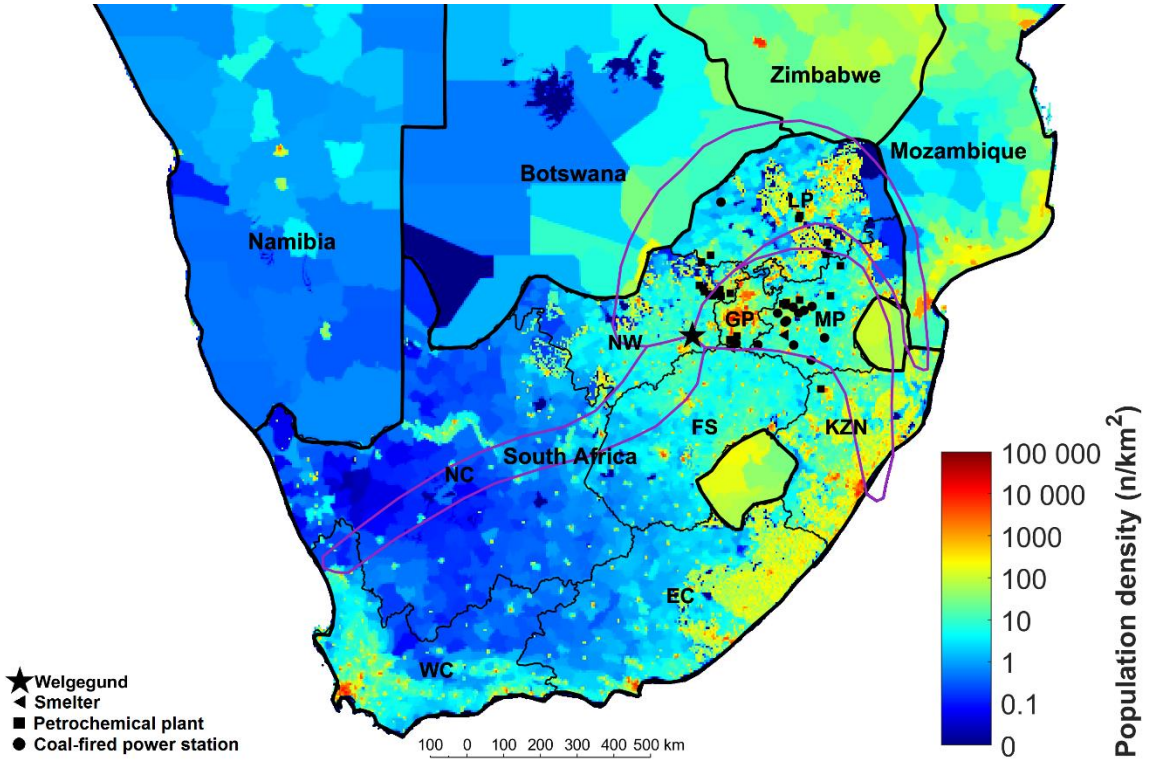

Figure 4.8: *Population density map of southern Africa (CIESIN et al., 2005) showing the locations of potential large Hg point sources in the South African interior. The polygons indicate the three main routes, or fetch regions, which were introduced in Figure 4.7. Province abbreviations: WC – Western Cape, NC – Northern Cape, EC – Eastern Cape, FS – Free State, NW – North West, GP – Gauteng Province, LP – Limpopo Province, MP – Mpumalanga Province, KZN – KwaZulu-Natal.*

As is evident from Figure 4.8, the majority of the southern African population live in the eastern half of the subcontinent. Areas with high population densities (1 000 – 10 000 people/km^2) in the eastern half of South Africa include the Johannesburg-Pretoria conurbation in Gauteng, as well as Pietermaritzburg and Durban in KwaZulu Natal. The Johannesburg-Pretoria conurbation is one of the 40 largest urban areas in the world, with a combined population of more than 10 million people. Conurbations of this size have been defined as megacities (Molina & Molina, 2004). Other cities with similar population densities (1 000 – 10 000 people/km^2) in neighbouring Zimbabwe and Mozambique include Harare (not shown on map), Bulawayo and Maputo. However, in general these populated areas are smaller and further apart than in South Africa. In contrast, the western portion of southern Africa, which include the Karoo and Kalahari in South Africa, Namibia and western Botswana, have much lower population densities (generally <10 people/km^2). The only exception is the Western Cape, where the Cape Town conurbation and numerous smaller cities/towns are located.

In addition to higher population densities to the east of Welgegund, most of the large anthropogenic point sources in the South African interior also occur to the east of Welgegund, as can be seen in Figure 4.8. These point sources include coal-fired power stations,

petrochemical plants and metallurgical smelters. More specifically, the closest large point sources to Welgegund are located in the Vaal Triangle Air-shed Priority Area (South Africa, 2005; Section 2.5), which lie almost directly east of the site. Here several petrochemical operations, one large power station and a couple of metallurgical smelters occur (Venter *et al.*, 2020) within a radius of about 15 km, approximately 100 km from Welgegund. The second nearest group of large point sources lie between north and north-northeast of Welgegund, within the Waterberg-Bojanala Priority Area (South Africa, 2012; Section 2.2). This group comprises of 11 pyro-metallurgical smelters, occurring within a radius of less than 60 km (Venter *et al.*, 2020). These point sources are located approximately 120 – 200 km from Welgegund.

As mentioned in Section 4.3.2, rainfall patterns affect not only the seasonality, but also the spatial distribution of open biomass burning events (Figure 4.5 and associated text), since precipitation directly influences the amount of biomass that is available for open biomass burning in any given location. It is evident from Figure 4.5 that the majority of open biomass burning occurred in the eastern and southern parts of southern Africa, since this is where the most productive biomes are found. In contrast, very few open biomass burning events were observed in the arid western part of the subcontinent. It is however important to note that, as previously mentioned, the peak open biomass burning period of the Grassland and Savannah biomes in the South African interior, where Welgegund is located, typically span from late local winter to early spring (Chiloane *et al.*, 2017; Booyens *et al.*, 2019; Maritz *et al.*, 2020). In contrast the peak open biomass burning period for the Fynbos biome in the southern parts of South Africa (Figure 4.5) typically span from late local spring to early autumn (Van Wilgen *et al.*, 2010). Hence, long-range transport from fires in the Fynbos biome could potentially affect TGM concentrations at Welgegund during late local spring to early autumn. However, such transport did not (Figure 4.7) and is unlikely to occur often.

Previously (Figure 4.7. and associated text), it was demonstrated that air masses arriving at Welgegund during the TGM measurement times, followed three main routes, or fetch regions. A southern African auto-generated source map (Vakkari *et.al.*, 2011; Section 3.4), for TGM measured at Welgegund, is presented in Figure 4.9. The afore-mentioned fetch regions were also superimposed on this map. TGM hourly means associated with the 1st fetch region had the lowest concentration range (approx. 1.3 – 1.8 ng.m^{-3}). This result seemed counterintuitive, since the 1st fetch region had the highest airmass overpass frequencies (Figure 4.7) and numerous large point sources were located therein (Figure 4.8). Additionally, this fetch region also had higher population densities (Figure 4.8) and more open biomass burning events (Figure 4.5), if compared to the 3rd fetch region, although it was lower on both counts than the 2nd fetch region. An auto-generated source map of O_3 concentrations measured at

Welgegund, during times when TGM data was available, is presented in Figure 4.10. This map helps explain the lowest TGM range associated with the 1st fetch region. As previously explained (Sections 2.3.3 and 4.3.1), O_3 and the $OH^{\bullet}$ resulting from the photolysis of O_3, both enhance removal of TGM from the troposphere (Lyman *et al.*, 2019). Therefore, the observed lower hourly mean TGM concentration range associated with the 1st fetch region (if compared to the other two fetch regions) could be attributed to the higher O_3 concentration range observed therein (Figures 4.9 and 4.10).

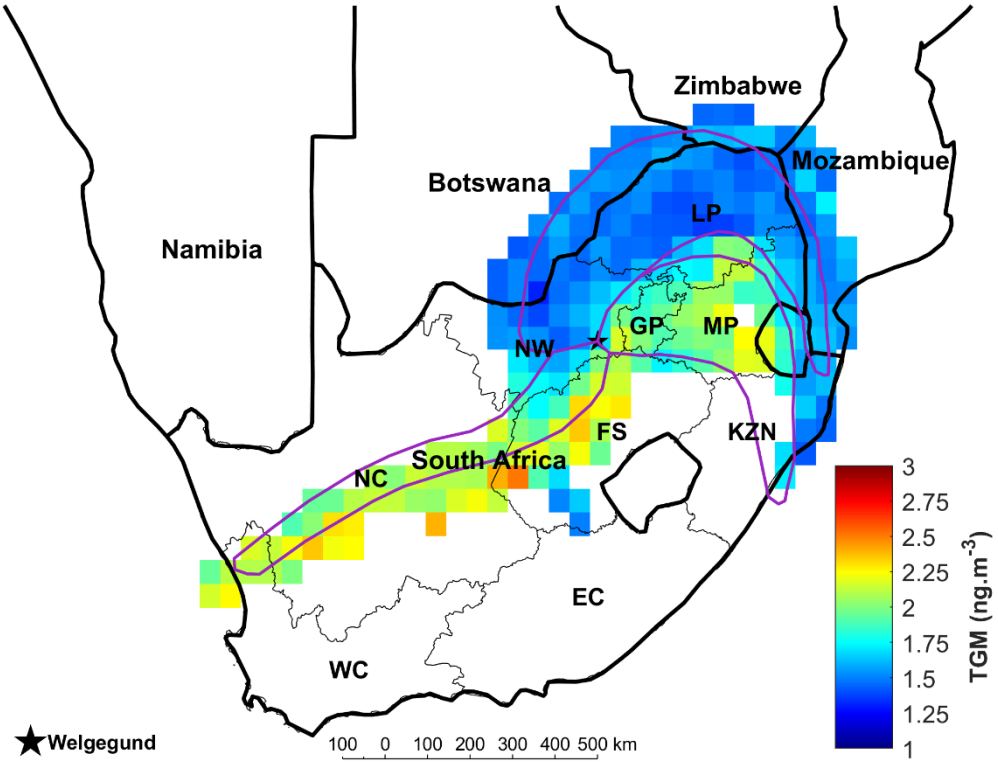

Figure 4.9: *Auto-generated source map of TGM concentrations measured at Welgegund during the measurement period. The polygons indicate the three main routes, or fetch regions, which were introduced in Figure 4.7. Province abbreviations: WC – Western Cape, NC – Northern Cape, EC – Eastern Cape, FS – Free State, NW – North West, GP – Gauteng Province, LP – Limpopo Province, MP – Mpumalanga Province, KZN – KwaZulu-Natal.*

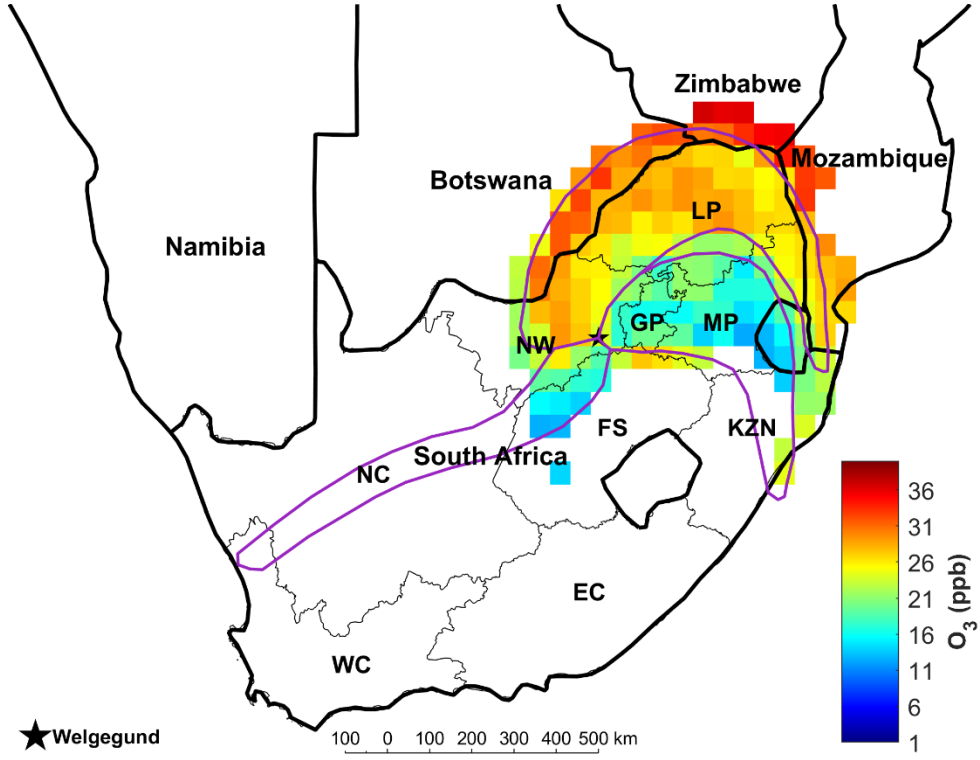

Figure 4.10: *Auto-generated source map of O_3 concentrations measured at Welgegund during the measurement period. The polygons indicate the three main routes, or fetch regions, which were introduced in Figure 4.7. Province abbreviations: WC – Western Cape, NC – Northern Cape, EC – Eastern Cape, FS – Free State, NW – North West, GP – Gauteng Province, LP – Limpopo Province, MP – Mpumalanga Province, KZN – KwaZulu-Natal.*

The TGM hourly mean concentrations for the 2nd fetch region (1.8 – 2.2 ng.m^{-3}) was significantly higher than that of the 1st. This was due to four contributing factors. Firstly, the highest population densities (Figure 4.8) occurred in the 2nd fetch region. Secondly, many large point sources were located closer to Welgegund than in the other fetch regions (Figure 4.8). Thirdly, the highest occurrence of open biomass burning amongst the fetch regions, were observed there (Figure 4.5). Lastly, a lower O_3 concentration range was also observed over this fetch region (Figure 4.10) if compared to the 1st fetch region. As stated, multiple times (e.g., Sections 2.3.3 and 4.3.1), O_3 (and $OH^{\bullet}$ derived from it) enhances TGM removal from the troposphere. The lower O_3 concentrations in this fetch region were due to the close proximity of the sources (i.e., less time for O_3 formation) and the polluted nature of the fetch region (Lourens *et al.*, 2011), which could lead to O_3 titration (Laban *et al.*, 2018).

Air masses from the 3rd fetch region had associated hourly mean TGM concentrations (approx. 1.8 – 2.6 ng.m^{-3}) similar to, although slightly higher than that of the 2nd fetch region. However, it is important to note that the 3rd fetch region had by far the lowest back trajectory overpass frequency of all three fetch regions (Figure 4.7) – hence it contributed least to the overall TGM measured at Welgegund. Also, almost no O_3 autogenerated source map data existed for this fetch region (Figure 4.10), due to O_3 data gaps that coincided with times when

back trajectories passed over this fetch region. Considering all the afore-mentioned, longer term data are required to more confidently state the TGM range associated with the 3rd fetch region and to explain it. Although a bit speculative, the extended time that air masses had spent over the continent in this fetch region could have contributed to the higher TGM concentrations. For instance, (Venter *et al.*, 2015) proved that GEM concentrations measured at the Cape Point Global Atmosphere Watch (CPT GAW) station increased if air masses spent more time over the continent (Figure 4.11). This is possibly as a result of two factors. Firstly, re-emission of previously deposited Hg from soils likely took place readily, due to the abundance of large, sparsely vegetated areas in the region (Figure 4.5). Secondly, the possibility that unmapped Hg-containing mineral deposits within the region contributed to the observed elevated TGM concentrations cannot be ruled out – Figure 2.4 (and associated text) discussed the distribution of Hg-containing mineral deposits in South Africa.

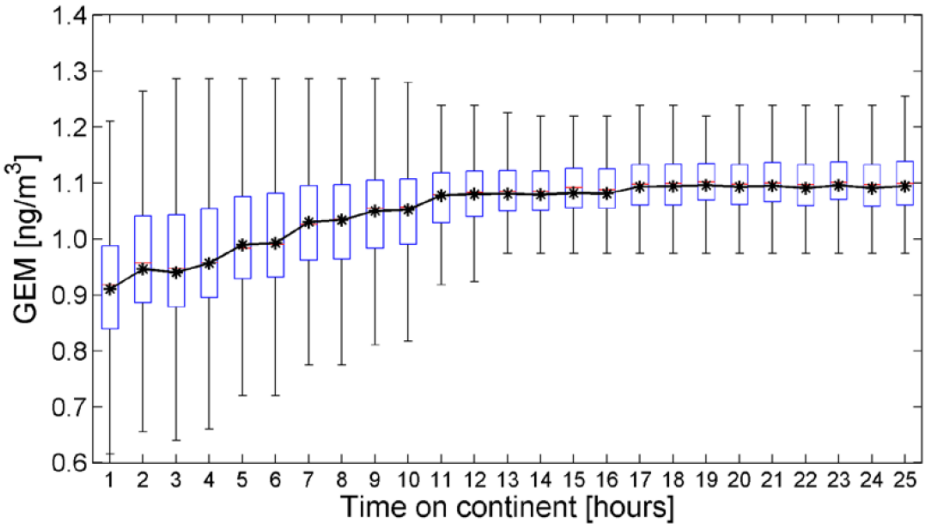

Figure 4.11: *Statistical distribution of GEM concentrations as a function of time spent over the continent. The red line indicates the median, the black star the mean, the top and bottom edges of the blue box the 25th and 75th percentiles and the black whiskers 1.5 times the interquartile range from the bottom or top of the box. Figure provided with permission by Venter et al. (2015).*

CHAPTER 5

Conclusion

In this chapter the main findings of the study are presented together with the project evaluation, in context of the study objectives. Perspectives on future atmospheric mercury (Hg) research are also discussed.

5.1 Main conclusions and project evaluation

In order to facilitate the project evaluation, the specific objectives originally stated in Section 1.2 are repeated here. This is followed by a consideration of the outcome of each objective, and the main conclusions related thereto.

Objective 1: *"Conduct total gaseous mercury (TGM) measurements at a suitable background site in the South African interior for at least one seasonal cycle."*

TGM measurements were conducted at the Welgegund Atmospheric Measurement Station between 17 September 2016 and 5 May 2017. The rationale for choosing Welgegund as the measurement site for this study was two-fold. Firstly, Welgegund is ideally positioned as a regional background site, since there are no large point sources or areas of high population density in close proximity to the site. Secondly, many other atmospheric species and meteorological parameters are continually monitored at Welgegund, which can be used to help explain/understand TGM observations. Unfortunately, due to multiple instances of instrument failure, as well as financial constraints, TGM data could not be obtained for a full seasonal cycle. However, the dataset spanned over 3 seasons: spring, summer and autumn. After data cleaning with a fit for purpose MATLAB® script, 30.53% of the dataset remained. Notwithstanding the relatively small dataset, the data still had significant value, considering the limited number of studies on TGM in the South African interior that have been published in the peer reviewed public domain, and the lack of such studies at background sites.

Objective 2: *"Calculate and contextualise the average TGM concentration at the selected site."*

The mean TGM concentration calculated at Welgegund over the measurement period was 1.68 ± 0.94 ng.m^{-3}. This value was compared to data from 28 other sites, located both in South Africa and internationally. The Welgegund TGM mean correlated well with data from other inland sites in South Africa, but was far below mean TGM concentrations for Sasolburg in the

Vaal Triangle Air-shed Priority Area and Elandsfontein in the Highveld Priority Area. This is not surprising, as TGM levels at both these sites are significantly influenced by emissions from nearby coal-fired power plants (Meyer, 2019). The Welgegund TGM mean was however elevated above concentrations measured at the coastal Cape Point Global Atmosphere Watch (CP GAW) station, which rather closely resemble the Southern Hemisphere background. Instead, the Welgegund TGM mean was more in range with Northern Hemisphere background concentrations, but still considerably lower than levels reported for heavily polluted Asian megacities. However, even though Welgegund is considered a regional background site, the TGM mean was about twice as high as measurements at true background sites in the Arctic, southern Indian Ocean and Antarctica.

Objective 3: *"Identify and explain temporal patterns in the measured TGM dataset."*

A clear diurnal trend in TGM concentrations was observed at Welgegund. This trend was evaluated in context of atmospheric species and meteorological parameters that were also measured at Welgegund. The overall average diurnal trend was found to be inversely related to ozone (O_3) concentrations, which in turn was also inversely related to relative humidity (RH) levels at the site. This indicated that the overall average trend is mostly explained by Hg oxidation and subsequent deposition. However, there was a relatively large peak in TGM concentrations during the late morning, which was not explained by the afore-mentioned chemistry. The peak was attributed to the breakdown of a low-level thermal inversion layer within the planetary boundary layer in the late morning, allowing downward mixing of air masses above the inversion – thus indicating transport of Hg from more distant sources to Welgegund.

Seasonal trends in TGM concentrations measured at Welgegund were also identified. Precipitation and open biomass burning were found to be the main drivers. Higher monthly mean TGM concentrations were observed during the dry season (May to middle October) than during the wet season (middle October to April). The dry season was characterised by low levels of precipitation, providing ample dry plant matter for open biomass burning. This subsequently resulted in increased TGM concentrations. In contrast, high levels of precipitation during the wet season facilitated the removal of TGM from the atmosphere through wet deposition, resulting in decreased TGM concentrations.

Objective 4: *"Identify and explain spatial patterns in the measured TGM dataset."*

Air mass backward trajectories were used to create an overlay back trajectory map for the periods when TGM data were available. From this map three main fetch regions for air mass travel, prior to being sampled at over Welgegund, were identified. The 1st route had the lowest associated TGM hourly mean concentration range, despite having the highest air mass

overpass frequency, relatively high population densities and numerous point sources located therein. The low TGM concentrations in this region was attributed to the oxidation of Hg^0 to Hg^{2+} by O_3 (which had the highest comparative concentration range over this fetch region) and $OH^{\bullet}$ (which forms from O_3), followed by the deposition of Hg^{2+} species. The 2nd fetch region had a significantly higher TGM hourly mean concentration range than the 1st. This was due to the highest population density, number of point sources and open biomass burning events occurring here, coupled with low O_3 concentrations. For reasons currently not fully understood, the 3rd fetch region had the highest associated TGM hourly mean concentration range, despite the lack of significant Hg sources therein. Although a bit speculative, it is thought that the extended time that air masses had spent over the continent in this fetch region may have contributed to the high TGM concentrations.

Objective 5: *"Provide insight into potential sources and/or contributing factors that influenced the TGM concentrations at the selected measurement site."*

The results of this study clearly indicated that TGM concentrations measured at Welgegund were strongly influenced by a number of factors, including population density, proximity of point sources, precipitation, biomes and open biomass burning, evolution of the PBL, time spent by an air mass over the continent, as well as chemical oxidation of Hg^0 by O_3 and $OH^{\bullet}$. The effect of these factors on TGM concentrations were already described in the outcome assessment of Objectives 3 and 4.

5.2 Future perspectives

Long-term measurements of atmospheric Hg at inland background sites in South Africa are extremely limited. Such measurements, in conjunction with data from the coastal CP GAW station, will be essential to reliably quantify background atmospheric Hg concentrations in South Africa, and contribute to meaningful discussions on the implementation of realistic Hg emission limits or ambient standards. This was recently highlighted by the Department of Science and Innovation through the establishment of the South African Mercury Network (SAMnet), a Hg monitoring network with five ambient measurement sites spread across the country (Mbatha & Martin, 2020). Long-term TGM measurements at Welgegund (initiated in 2021) form part of this plan. Such measurements will help to address the uncertainties indicated in the current study (e.g., the 3rd fetch region that had the highest associated TGM hourly mean concentration range, despite the lack of significant Hg sources therein). A statistical approach towards the analysis of such long-term measurements (e.g. using multiple linear regression) will also allow deeper insight into the degree of influence that the parameters

identified in this study (e.g. O_3, RH, precipitation and open biomass burning) have on atmospheric Hg concentrations.

Studying ambient atmospheric Hg concentrations alone is not sufficient to understand atmospheric Hg and its impact in South Africa. Several additional aspects are required. Firstly, detailed atmospheric Hg emission inventories need to be established for South Africa and made available in the peer reviewed public domain, to help interpret future measurements and/or to be used in modelling studies. Measurements of halogens (currently very limited in South Africa), and radicals (no such measurements currently in South Africa) need to be initiated, since these species are critical in understanding atmospheric Hg oxidation. Oxidation makes atmospheric Hg soluble, which significantly enhances wet deposition. Studies on wet and dry deposition of atmospheric Hg need to be undertaken, since deposition is the first step towards bioaccumulation. Currently it is foreseen that wet deposition measurements of Hg at Welgegund will be initiated in 2021.

Annexure A

Excerpt from a typical raw data file illustrating the format in which calibration and sample data is stored by the Tekran® 2537B ambient Hg vapour analyser.

```
20160920005009 Date       Time       Typ   C Stat   AdTim  Vol   Bl     BlDev  MaxV  Area    ng/m3
20160920002012 16-09-20 00:19:23 CLN   A  NP  0      0     .00  0.148  .036  .000        0    0.000
20160920002241 16-09-20 00:21:52 CLN   B  OK  0    148    3.75  0.148  .045 0.150     4403    0.000
20160920002740 16-09-20 00:25:03 ZERO  A  OK  0    300    7.40  0.148  .041 0.150     5844    0.000
20160920003240 16-09-20 00:30:03 ZERO  B  OK  0    300    7.51  0.148  .042 0.150     5987    0.000
20160920003740 16-09-20 00:35:03 SPAN  A  OK  0    300    7.50  0.148  .038 0.334   617630   13.968
20160920004240 16-09-20 00:40:03 SPAN  B  OK  0    300    7.51  0.148  .046 0.330   610276   13.968
20160920004320 -
20160920004320 CALIBRATION:  S/N:0415    H/W: 3.30   S/W: 1.14      16-09-20   00:42:32
20160920004320 -
20160920004320 ZERO:  A
20160920004320 Sample  :   300 sec  |  BlArea  :   5844
20160920004320 Volume  :  7.40 l    |  BlCorr  :    790/l
20160920004320 Baseline: 0.148 V    |  PkMax   : 0.150 V
20160920004321 Bl StDev:   .04 mv   |  PkWid   :   6.1 sec
20160920004321 Start   : 16-09-20      00:25:03
20160920004321 -
20160920004321 ZERO:  B
20160920004321 Sample  :   300 sec  |  BlArea  :   5987
20160920004321 Volume  :  7.51 l    |  BlCorr  :    798/l
20160920004321 Baseline: 0.148 V    |  PkMax   : 0.150 V
20160920004321 Bl StDev:   .04 mv   |  PkWid   :   6.1 sec
20160920004321 Start   : 16-09-20      00:30:03
20160920004321 -
20160920004321 SPAN:  A     SOURCE
20160920004321 Sample  :   300 sec  |  Area    : 617630
```

20160920004321 Volume : 7.50 l | AdjArea : 611708 *

20160920004321 HgAmt : 104.8pg | RespFctr:5839140

20160920004321 Baseline: 0.148 V | PkMax : 0.334 V

20160920004321 Bl StDev: .04 mv | PkWid : 15.8 sec

20160920004321 Start : 16-09-20 00:35:03

20160920004321 -

20160920004321 SPAN: B SOURCE

20160920004321 Sample : 300 sec | Area : 610276

20160920004321 Volume : 7.51 l | AdjArea : 604288 *

20160920004321 HgAmt : 104.8pg | RespFctr:5768310

20160920004321 Baseline: 0.148 V | PkMax : 0.330 V

20160920004321 Bl StDev: .05 mv | PkWid : 15.7 sec

20160920004321 Start : 16-09-20 00:40:03

20160920004321 -

20160920004821

20160920005009 -

	Date	Time	Typ	C	Stat	AdTim	Vol	Bl	BlDev	MaxV	Area	ng/m3
20160920005009	16-09-20	00:49:20	CLN	A	NP	0	0	.00	0.148	.042	.000	0	0.000
20160920005238	16-09-20	00:51:49	CLN	B	OK	0	148	3.75	0.148	.040	0.149	3695	0.000
20160920005737	16-09-20	00:55:00	CONT	A	OK	0	300	7.46	0.148	.045	0.172	84420	1.938
20160920010237	16-09-20	01:00:00	CONT	B	OK	0	300	7.51	0.148	.035	0.171	84445	1.950
20160920010737	16-09-20	01:05:00	CONT	A	OK	0	300	7.50	0.148	.049	0.172	82590	1.886
20160920011237	16-09-20	01:10:00	CONT	B	OK	0	300	7.50	0.148	.042	0.171	82022	1.895
20160920011737	16-09-20	01:15:00	CONT	A	OK	0	300	7.50	0.148	.041	0.172	82427	1.882
20160920012237	16-09-20	01:20:00	CONT	B	OK	0	300	7.50	0.148	.043	0.171	82067	1.896
20160920012737	16-09-20	01:25:00	CONT	A	OK	0	300	7.50	0.148	.042	0.172	83355	1.903
20160920013237	16-09-20	01:30:00	CONT	B	OK	0	300	7.51	0.148	.048	0.171	79998	1.848
20160920013737	16-09-20	01:35:00	CONT	A	OK	0	300	7.50	0.148	.040	0.172	82974	1.895
20160920014237	16-09-20	01:40:00	CONT	B	OK	0	300	7.51	0.148	.042	0.171	82118	1.897

Bibliography

Amos, H.M., Jacob, D.J., Holmes, C., Fisher, J.A., Wang, Q., Yantosca, R.M., Corbitt, E.S., Galarneau, E., Rutter, A. & Gustin, M. 2012. Gas-particle partitioning of atmospheric Hg (II) and its effect on global mercury deposition. *Atmospheric Chemistry and Physics*, 12:591-603.

Andreae, M.O. 2007. Atmospheric aerosols versus greenhouse gases in the twenty-first century. *Philosophical Transactions of the Royal Society A: Mathematical, Physical and Engineering Sciences*, 365(1856):1915-1923.

Andreoli, V. & Sprovieri, F. 2017. Genetic aspects of susceptibility to mercury toxicity: an overview. *International journal of environmental research and public health*, 14(1):93.

Angot, H., Barret, M., Magand, O., Ramonet, M. & Dommergue, A. 2014. A 2-year record of atmospheric mercury species at a background Southern Hemisphere station on Amsterdam Island. *Atmospheric Chemistry and Physics*, 14:11461-11473.

Angot, H., Dion, I., Vogel, N., Legrand, M., Magand, O. & Dommergue, A. 2016. Multi-year record of atmospheric mercury at Dumont d'Urville, East Antarctic coast: Continental outflow and oceanic influences. *Atmospheric Chemistry and Physics*, 16:8265-8279.

Archibald, S., Roy, D., van Wilgen, B. & Scholes, R. 2009. What limits fire? An examination of drivers of burnt area in Southern Africa. *Global Change Biology*, 15:613-630.

Ariya, P.A., Khalizov, A. & Gidas, A. 2002. Reactions of Gaseous Mercury with Atomic and Molecular Halogens: Kinetics, Product Studies, and Atmospheric Implications. *The Journal of Physical Chemistry A*, 106(32):7310-7320.

Atkinson, R. 2000. Atmospheric chemistry of VOCs and NOx. *Atmospheric Environment*, 34(12):2063-2101.

Baker, P.G.L., Brunke, E.G., Slemr, F., Crouch, A. M. 2002. Atmospheric mercury measurements at Cape Point, South Africa. *Atmospheric Environment*, 36(14):2459-2465.

Bank, M.S. 2012. Mercury in the environment: pattern and process. 1st ed. Berkeley: University of California Press.

Barber, J.L., Thomas, G.O., Kerstiens, G. & Jones, K.C. 2004. Current issues and uncertainties in the measurement and modelling of air–vegetation exchange and within-plant processing of POPs. *Environmental Pollution*, 128(1):99-138.

Beckett, K.P., Freer-Smith, P. & Taylor, G. 1998. Urban woodlands: their role in reducing the effects of particulate pollution. *Environmental Pollution*, 99(3):347-360.

Belelie, M.D., Piketh, S.J., Burger, R.P., Venter, A.D. & Naidoo, M. 2019. Characterisation of ambient Total Gaseous Mercury concentrations over the South African Highveld. *Atmospheric Pollution Research*, 10(1):12-23.

Beukes, J.P., Venter, A.D., Josipovic, M., Van Zyl, P.G., Vakkari, V., Jaars, K., Dunn, M. & Laakso, L. 2015. 'Chapter 6: Automated continuous air monitoring', in Forbes, P. (ed.), *Monitoring of air pollutants – Sampling, sample, preparation and analytical techniques*, Elsevier. p. 183-208.

Bieser, J., Slemr, F., Ambrose, J., Brenninkmeijer, C., Brooks, S., Dastoor, A., DeSimone, F., Ebinghaus, R., Gencarelli, C.N., Geyer, B., Gratz, L.E., Hedgecock, I.M., Jaffe, D., Kelley, P., Lin, C.J., Jaegle, L., Matthias, V., Ryjkov, A., Selin, N.E., Song, S., Travnikov, O., Weigelt, A., Luke, W., Ren, X., Zahn, A., Yang, X., Zhu, Y. & Pirrone, N. 2017. Multi-model study of mercury dispersion in the atmosphere: vertical and interhemispheric distribution of mercury species. *Atmospheric Chemistry and Physics*, 17(11):6925-6955.

Bieser, J., Angot, H., Slemr, F. & Martin, L. 2020. Atmospheric mercury in the Southern Hemisphere – Part 2: Source apportionment analysis at Cape Point station, South Africa. *Atmospheric Chemistry and Physics*, 20(17):10427-10439.

Bjørklund, G., Dadar, M., Mutter, J. & Aaseth, J. 2017. The toxicology of mercury: Current research and emerging trends. *Environmental research*, 159:545-554.

Bjørklund, G., Chirumbolo, S., Dadar, M., Pivina, L., Lindh, U., Butnariu, M. & Aaseth, J. 2019. Mercury exposure and its effects on fertility and pregnancy outcome. *Basic & Clinical Pharmacology & Toxicology*, 125(4):317-327.

Booyens, W., Beukes, J.P., Van Zyl, P.G., Ruiz-Jimenez, J., Kopperi, M., Riekkola, M.-L., Josipovic, M., Vakkari, V. & Laakso, L. 2019. Assessment of polar organic aerosols at a regional background site in southern Africa. *Journal of Atmospheric Chemistry*, 76(2):89-113.

Brimblecombe, P. 1995. Air composition & chemistry. 2nd ed. Cambridge: University Press.

Brunke, E., Ebinghaus, R., Kock, H., Labuschagne, C. & Slemr, F. 2012. Emissions of mercury in southern Africa derived from long-term observations at Cape Point, South Africa. *Atmospheric Chemistry & Physics*, 12:7465-7474.

Brunke, E., Labuschagne, C. & Slemr, F. 2001. Gaseous mercury emissions from a fire in the Cape Peninsula, South Africa, during January 2000. *Geophysical Research Letters*, 28(8):1483-1486.

Cairncross, B. & Dixon, R. 1995. Minerals of South Africa. Johannesburg: Geological Society of South Africa.

Calvert, J.G. & Lindberg, S.E. 2005. Mechanisms of mercury removal by O3 and OH in the atmosphere. *Atmospheric Environment*, 39(18):3355-3367.

Chiloane, K.E., Beukes, J.P., Van Zyl, P.G., Maritz, P., Vakkari, V., Josipovic, M., Venter, A.D., Jaars, K., Tiitta, P. & Kulmala, M. 2017. Spatial, temporal and source contribution assessments of black carbon over the northern interior of South Africa. *Atmospheric Chemistry and Physics*, 17:6177-6196.

Choi, E.-M., Kim, S.-H., Holsen, T.M. & Yi, S.-M. 2009. Total gaseous concentrations in mercury in Seoul, Korea: Local sources compared to long-range transport from China and Japan. *Environmental Pollution*, 157(3):816-822.

CIESIN, FAO & CIAT. 2005. Gridded Population of the World: Future Estimates (GPWFE). http://sedac.ciesin.columbia.edu/gpw Date of access: 2010.

Cobbett, F.D., Steffen, A., Lawson, G. & Van Heyst, B.J. 2007. GEM fluxes and atmospheric mercury concentrations (GEM, RGM and Hgp) in the Canadian Arctic at Alert, Nunavut, Canada (February-June 2005). *Atmospheric Environment*, 41(31):6527-6543.

Cole, A., Steffen, A., Eckley, C., Narayan, J., Pilote, M., Tordon, R., Graydon, J., St.Louis, V., Xu, X. & Branfireum, B. 2014. A Survey of Mercury in Air and Precipitation across Canada: Patterns and Trends. *Atmosphere*, 5:635-668.

Connell, D.W. 2005. Basic concepts of environmental chemistry: CRC Press.

Council for Geoscience (Cartographer). (2019). Geological Map of The Republic of South Africa And the Kingdoms of Lesotho And Swaziland. Retrieved from https://geoscience.org.za/cgs/

D'Amore, F., Bencardino, M., Cinnirella, S., Sprovieri, F. & Pirrone, N. 2015. Data quality through a web-based QA/QC system: implementation for atmospheric mercury data from the Global Mercury Observation System. *Environmental Science: Processes & Impacts*, 17(8):1482-1491.

Dabrowski, J.M., Ashton, P.J., Murray, K., Leaner, J.J. & Mason, R.P. 2008. Anthropogenic mercury emissions in South Africa: Coal combustion in power plants. *Atmospheric Environment*, 42(27):6620-6626.

DEA. 2011. Inventory of mercury releases in South Africa. Tshwane.

Dibble, T.S., Zelie, M.J. & Mao, H. 2012. Thermodynamics of reactions of ClHg and BrHg radicals with atmospherically abundant free radicals. *Atmospheric Chemistry and Physics*, 12(21):10271-10279.

Diéguez, M.C., Bencardino, M., García, P.E., D'Amore, F., Castagna, J., De Simone, F., Soto Cárdenas, C., Ribeiro Guevara, S., Pirrone, N. & Sprovieri, F. 2019. A multi-year record of atmospheric mercury species at a background mountain station in Andean Patagonia (Argentina): Temporal trends and meteorological influence. *Atmospheric Environment*, 214:116819.

Draxler, R. & Hess, G. 1997. Description of the HYSPLIT_4 modelling system. *NOAA Tech. Mem. ERL ARL-224*.

Driscoll, C.T., Mason, R.P., Chan, H.M., Jacob, D.J. & Pirrone, N. 2013. Mercury as a Global Pollutant: Sources, Pathways, and Effects. *Environmental science & technology*, 47(10):4967-4983.

Duan, L., Wang, X., Wang, D., Duan, Y., Cheng, N. & Xiu, G. 2017. Atmospheric mercury speciation in Shanghai, China. *Science of The Total Environment*, 578:460-468.

Ebinghaus, R., Kock, H., Labuschagne, C., Brunke, E.G., Slemr, F. 2010. Atmospheric mercury measurements at Cape Point, South Africa. *Clean Air Journal = Tydskrif vir Skoon Lug*, 18(1):17-21.

Ekino, S., Susa, M., Ninomiya, T., Imamura, K. & Kitamura, T. 2007. Minamata disease revisited: An update on the acute and chronic manifestations of methyl mercury poisoning. *Journal of the neurological sciences*, 262:131-144.

Enrico, M., Le Roux, G., Heimbürger, L.-E., Van Beek, P., Souhaut, M., Chmeleff, J.r. & Sonke, J.E. 2017. Holocene atmospheric mercury levels reconstructed from peat bog mercury stable isotopes. *Environmental science & technology*, 51(11):5899-5906.

Esdaile, L.J. & Chalker, J.M. 2018. The Mercury Problem in Artisanal and Small-Scale Gold Mining. *Chemistry – A European Journal*, 24(27):6905-6916.

Feng, X., Li, P., Qiu, G., Wang, S., Li, G., Shang, L., Meng, B., Jiang, H., Bai, W., Li, Z. & Fu, X. 2008. Human Exposure To Methylmercury through Rice Intake in Mercury Mining Areas, Guizhou Province, China. *Environmental science & technology*, 42(1):326-332.

Gaffney, J. 2014. In-depth review of atmospheric mercury: Sources, transformations, and potential sinks. *Energy and Emission Control Technologies*, 2:1-21.

Gardoni, D., Vailati, A. & Canziani, R. 2012. Decay of Ozone in Water: A Review. *Ozone Science and Engineering*, 34:233.

Garnham, B.L. & Langerman, K.E. 2016. Mercury emissions from South Africa's coal-fired power stations. *Clean Air Journal = Tydskrif vir Skoon Lug*, 26(2):14-20.

GDAS. 2019. Archives. ftp://arlftp.arlhq.noaa.gov/pub/archives/gdas1/ Date of access: 15 Aug 2019.

Gencarelli, C.N., Bieser, J., Carbone, F., De Simone, F., Hedgecock, I.M., Matthias, V., Travnikov, O., Yang, X. & Pirrone, N. 2017. Sensitivity model study of regional mercury dispersion in the atmosphere. *Atmospheric Chemistry and Physics*, 17(1):627-643.

Gierens, R.T., Henriksson, S., Josipovic, M., Vakkari, V., van Zyl, P.G., Beukes, J.P., Wood, C.R. & O'Connor, E.J. 2019. Observing continental boundary-layer structure and evolution over the South African savannah using a ceilometer. *Theoretical and Applied Climatology*, 136(1):333-346.

Goodsite, M.E., Plane, J.M.C. & Skov, H. 2004. A Theoretical Study of the Oxidation of Hg0 to $HgBr_2$ in the Troposphere. *Environmental science & technology*, 38(6):1772-1776.

Gray, J.E., Hines, M.E., Higueras, P.L., Adatto, I. & Lasorsa, B.K. 2004. Mercury speciation and microbial transformations in mine wastes, stream sediments, and surface waters at the Almadén mining district, Spain. *Environmental science & technology*, 38(16):4285-4292.

Griggs, T., Liu, L., Talbot, R.W., Torres, A. & Lan, X. 2020. Comparison of atmospheric mercury speciation at a coastal and an urban site in Southeastern Texas, USA. *Atmosphere*, 11(1).

Gustin, M.S., Amos, H.M., Huang, J., Miller, M.B. & Heidecorn, K. 2015. Measuring and modeling mercury in the atmosphere: a critical review. *Atmospheric Chemistry and Physics*, 15(10):5697-5713.

Gworek, B., Dmuchowski, W., Baczewska, A.H., Brągoszewska, P., Bemowska-Kałabun, O. & Wrzosek-Jakubowska, J. 2017. Air Contamination by Mercury, Emissions and Transformations—a Review. *Water, Air, & Soil Pollution*, 228(4):123.

Harrison, R.M. 1999. Understanding Our Environment: An Introduction to Environmental Chemistry and Pollution. 3rd ed. Cambridge: The Royal Society of Chemistry.

Holmes, C.D., Jacob, D.J. & Yang, X. 2006. Global lifetime of elemental mercury against oxidation by atomic bromine in the free troposphere. *Geophysical Research Letters*, 33(20).

Holmes, C.D., Jacob, D.J., Mason, R.P. & Jaffe, D.A. 2009. Sources and deposition of reactive gaseous mercury in the marine atmosphere. *Atmospheric Environment*, 43(14):2278-2285.

Horowitz, H.M., Jacob, D.J., Zhang, Y., Dibble, T.S., Slemr, F., Amos, H.M., Schmidt, J.A., Corbitt, E.S., Marais, E.A. & Sunderland, E.M. 2017. A new mechanism for atmospheric mercury redox chemistry: implications for the global mercury budget. *Atmospheric Chemistry and Physics*, 17(10):6353-6371.

Howard, D., Nelson, P.F., Edwards, G.C., Morrison, A.L., Fisher, J.A., Ward, J., Harnwell, J., van der Schoot, M., Atkinson, B., Chambers, S.D., Griffiths, A.D., Werczynski, S. & Williams, A.G. 2017. Atmospheric mercury in the Southern Hemisphere tropics: seasonal and diurnal variations and influence of inter-hemispheric transport. *Atmospheric Chemistry and Physics*, 17(18):11623-11636.

Jaars, K., Beukes, J.P., van Zyl, P.G., Venter, A.D., Josipovic, M., Pienaar, J.J., Vakkari, V., Aaltonen, H., Laakso, H., Kulmala, M., Tiitta, P., Guenther, A., Hellén, H., Laakso, L. &

Hakola, H. 2014. Ambient aromatic hydrocarbon measurements at Welgegund, South Africa. *Atmospheric Chemistry and Physics*, 14(13):7075-7089.

Jaars, K., Zyl, P.G., Beukes, J.P., Hellén, H., Vakkari, V., Josipovic, M., Venter, A., Räsänen, M., Knoetze, L., Cilliers, D., Siebert, S., Kulmala, M., Rinne, J., Guenther, A., Laakso, L. & Hakola, H. 2016. Measurements of biogenic volatile organic compounds at a grazed savannah-grassland-agriculture landscape in South Africa. *Atmospheric Chemistry and Physics Discussions*:1-46.

Jia, L. & Xu, Y. 2014. Effects of Relative Humidity on Ozone and Secondary Organic Aerosol Formation from the Photooxidation of Benzene and Ethylbenzene. *Aerosol Science and Technology*, 48(1):1-12.

Jiskra, M., Sonke, J.E., Obrist, D., Bieser, J., Ebinghaus, R., Myhre, C.L., Pfaffhuber, K.A., Wängberg, I., Kyllönen, K., Worthy, D., Martin, L.G., Labuschagne, C., Mkololo, T., Ramonet, M., Magand, O., Dommergue, A. 2018. A vegetation control on seasonal variations in global atmospheric mercury concentrations. *Nature Geoscience*, 11(4):244-250.

Kampa, M. & Castanas, E. 2008. Human health effects of air pollution. *Environmental Pollution*, 151(2):362-367.

Karthik, R., Paneerselvam, A., Ganguly, D., Hariharan, G., Srinivasalu, S., Purvaja, R. & Ramesh, R. 2017. Temporal variability of atmospheric Total Gaseous Mercury and its correlation with meteorological parameters at a high-altitude station of the South India. *Atmospheric Pollution Research*, 8(1):164-173.

Kentisbeer, J., Leeson, S.R., Clark, T., Malcolm, H.M. & Cape, J.N. 2015. Influences on and patterns in total gaseous mercury (TGM) at Harwell, England. *Environmental Science: Processes and Impacts*, 17(3):586-595.

Kim, K.-H., Jahan, S.A. & Kabir, E. 2013. A review on human health perspective of air pollution with respect to allergies and asthma. *Environment International*, 59(Supplement C):41-52.

Kim, M.-K. & Zoh, K.-D. 2013. Erratum: Fate and Transport of Mercury in Environmental Media and Human Exposure. *Journal of preventive medicine and public health = Yebang Uihakhoe chi*, 46:211.

Kocman, D., Horvat, M. & Wilson, S. 2013. 'Chapter 4: Global Releases of Mercury to Aquatic Environments', in *Technical Background Report for the Global Mercury* Assessment, Arctic Monitoring and Assessment Programme, Oslo, Norway/UNEP Chemicals Branch, Geneva, Switzerland. p. vi + 263.

Kyllonen, K., Paatero, J., Aalto, T. & Hakola, H. 2014. Nationwide survey of airborne mercury in Finland. *Boreal Environment Research*, 19:SS355+.

Laban, T.L., Van Zyl, P.G., Beukes, J.P., Vakkari, V., Jaars, K., Borduas-Dedekind, N., Josipovic, M., Thompson, A.M., Kulmala, M. & Laakso, L. 2018. Seasonal influences on surface ozone variability in continental South Africa and implications for air quality. *Atmospheric Chemistry and Physics*.

Leaner, J. 2007. Focus on CSIR Research in Water Resources: South African Mercury Assesment (SAMA) Programme: CSIR.

Leaner, J.J., Dabrowski, J.M., Mason, R.P., Resane, T., Richardson, M., Ginster, M., Gericke, G., Petersen, C.R., Masekoameng, E. & Ashton, P.J. 2009. 'Chapter 5: Mercury emissions from point sources in South Africa', in *Mercury Fate and Transport in the Global Atmosphere*, Springer. p. 113-130.

Lin, C.-J. & Pehkonen, S.O. 1997. Aqueous free radical chemistry of mercury in the presence of iron oxides and ambient aerosol. *Atmospheric Environment*, 31(24):4125-4137.

Lin, C.-J. & Pehkonen, S.O. 1998. Oxidation of elemental mercury by aqueous chlorine ($HOCl/OCl^-$): Implications for tropospheric mercury chemistry. *Journal of Geophysical Research*, 103:28,093-028,102.

Lin, C.-J. & Pehkonen, S.O. 1999. The chemistry of atmospheric mercury: a review. *Atmospheric Environment*, 33(13):2067-2079.

Lindberg, S. & Stratton, W. 1998. Atmospheric mercury speciation: Concentrations and behavior of reactive gaseous mercury in ambient air. *Environmental science & technology*, 32(1):49-57.

Lindberg, S, Brooks, S., Lin, C.J., Scott, K.J., Landis, M.S., Stevens, R.K., Goodsite, M. & Richter, A. 2002. Dynamic Oxidation of Gaseous Mercury in the Arctic Troposphere at Polar Sunrise. *Environmental science & technology*, 36(6):1245-1256.

Lindberg, S., Bullock, R., Ebinghaus, R., Engstrom, D., Feng, X., Fitzgerald, W., Pirrone, N., Prestbo, E. & Seigneur, C. 2007. A synthesis of progress and uncertainties in attributing the sources of mercury in deposition. *Ambio*:19-32.

Lindqvist, O. & Rodhe, H. 1985. Atmospheric mercury-a review. *Tellus Series B Chemical and Physical Meteorology B*, 37:136-159.

Lourens, A.S., Beukes, J.P., van Zyl, P.G., Fourie, G.D., Burger, J.W., Pienaar, J.J., Read, C.E. & Jordaan, J.H. 2011. Spatial and temporal assessment of gaseous pollutants in the Highveld of South Africa. *South African Journal of Science*, 107(1/2):55-62.

Luo, H., Cheng, Q. & Pan, X. 2020. Photochemical behaviors of mercury (Hg) species in aquatic systems: A systematic review on reaction process, mechanism, and influencing factor. *Science of The Total Environment*, 720:137540.

Lyman, S.N. & Gustin, M.S. 2009. Determinants of atmospheric mercury concentrations in Reno, Nevada, U.S.A. *Science of The Total Environment*, 408(2):431-438.

Lyman, S., Cheng, I., Gratz, L., Weiss, P. & Zhang, L. 2019. An updated review of atmospheric mercury. *Science of The Total Environment*, 707:135575.

Maritz, P., Beukes, J.P., Van Zyl, P.G., Liousse, C., Gardrat, E., Ramandh, A. & Mkhatshwa, G.V. 2020. Temporal and source assessments of organic and elemental carbon at sites in the northern South African interior. *Journal of Atmospheric Chemistry*, 76:263-287.

Marumoto, K., Hayashi, M. & Takami, A. 2015. Atmospheric mercury concentrations at two sites in the Kyushu Islands, Japan, and evidence of long-range transport from East Asia. *Atmospheric Environment*, 117:147-155.

Marusczak, N., Castelle, S., de Vogüé, B., Knoery, J. & Cossa, D. 2016. Seasonal variations of total gaseous mercury at a French coastal mediterranean site. *Aerosol and Air Quality Research*, 16(1):46-60.

Masekoameng, K.E., Leaner, J. & Dabrowski, J. 2010. Trends in anthropogenic mercury emissions estimated for South Africa during 2000–2006. *Atmospheric Environment*, 44(25):3007-3014.

Mbatha, N. & Martin, L. 2020. Atmospheric modelling over South Africa. In *Multimedia modelling of global mercury movement* [Webinar].

http://www.mercuryconvention.org/Portals/11/documents/Presentations/Nov17_Nkanyiso_Mbatha.pdf Date of access: 11 December 2020.

Meng, Q.Y., Qian, X.L., Chen, M., Zhao, L., Feng, X.B. & Bo, M. 2018. Biogeochemical cycle of mercury in rice paddy ecosystem: A critical review. *Chinese Journal of Ecology*, 37:1556-1573.

Mészáros, E. 1981. Atmospheric Chemistry: Fundamental Aspects. 1st ed. Vol. 11. Amsterdam: Elsevier Scientific Publishing Company.

Meyer, R. 2019. Ambient mercury concentrations at industrially influenced sites on the Highveld. North-West University.

Minamata Convention on Mercury. Opened for signature 10 October 2013, entered into force 16 August 2017. Available from: https://treaties.un.org/doc/Publication/MTDSG/Volume%20II/Chapter%20XXVII/XXVII-17.en.pdf Date of access: 3 December 2020.

Mindat.org. 2020. South Africa. https://www.mindat.org/loc-14468.html Date of access: 15 September 2020.

Molina, M.J. & Molina, L.T. 2004. Megacities and atmospheric pollution. *Journal of the Air & Waste Management Association*, 54(6):644-680.

Mucina, L. & Rutherford, M.C. 2006. The vegetation of South Africa, Lesotho and Swaziland. 1st ed. Pretoria: South African Biodiversity Institute.

Müller, D., Wip, D., Warneke, T., Holmes, C.D., Dastoor, A. & Notholt, J. 2012. Sources of atmospheric mercury in the tropics: Continuous observations at a coastal site in Suriname. *Atmospheric Chemistry and Physics*, 12(16):7391-7397.

Munthe, J. 1992. The aqueous oxidation of elemental mercury by ozone. *Atmospheric Environment Part A, General Topics*, 26(8):1461-1468.

Naiker, Y., Diab, R.D., Zunckel, M. & Hayes, E.T. 2012. Introduction of local Air Quality Management in South Africa: overview and challenges. *Environmental Science & Policy*, 17:62-71.

Nriagu, J.O. 1994. Mechanistic steps in the photoreduction of mercury in natural waters. *Science of The Total Environment*, 154(1):1-8.

Pacyna, E.G., Pacyna, J.M., Steenhuisen, F. & Wilson, S. 2006. Global anthropogenic mercury emission inventory for 2000. *Atmospheric Environment*, 40(22):4048-4063.

Pacyna, J.M., Travnikov, O., Simone, F.D., Hedgecock, I.M., Sundseth, K., Pacyna, E.G., Steenhuisen, F., Pirrone, N., Munthe, J. & Kindbom, K. 2016. Current and future levels of mercury atmospheric pollution on a global scale. *Atmospheric Chemistry and Physics*, 16(19):12495-12511.

Pal, B. & Ariya, P.A. 2004. Gas-Phase HO•-Initiated Reactions of Elemental Mercury: Kinetics, Product Studies, and Atmospheric Implications. *Environmental science & technology*, 38(21):5555-5566.

Pehkonen, S.O. & Lin, C.-J. 1998. Aqueous photochemistry of mercury with organic acids. *Journal of the Air & Waste Management Association (Air & Waste Management Association)*, 48:144-150.

Pfaffhuber, K.A., Berg, T., Hirdman, D. & Stohl, A. 2012. Atmospheric mercury observations from Antarctica: seasonal variation and source and sink region calculations. *Atmospheric Chemistry and Physics*, 12(7):3241-3251.

Pirrone, N., Cinnirella, S., Feng, X., Finkelman, R., Friedli, H., Leaner, J., Mason, R., Mukherjee, A., Stracher, G. & Streets, D. 2010. Global mercury emissions to the atmosphere from anthropogenic and natural sources. *Atmospheric Chemistry and Physics*, 10(13):5951-5964.

Poissant, L., Pilote, M., Beauvais, C., Constant, P. & Zhang, H.H. 2005. A year of continuous measurements of three atmospheric mercury species (GEM, RGM and Hgp) in southern Québec, Canada. *Atmospheric Environment*, 39(7):1275-1287.

Ramanathan, V. & Feng, Y. 2009. Air pollution, greenhouse gases and climate change: Global and regional perspectives. *Atmospheric Environment*, 43(1):37-50.

Read, K., Neves, L., Carpenter, L., Lewis, A., Fleming, Z. & Kentisbeer, J. 2017. Four years (2011–2015) of total gaseous mercury measurements from the Cape Verde Atmospheric Observatory. *Atmospheric Chemistry and Physics*, 17:5393-5406.

Renzoni, A., Zino, F. & Franchi, E. 1998. Mercury levels along the food chain and risk for exposed populations. *Environmental research*, 77(2):68-72.

Roy, D.P., Boschetti, L., Justice, C.O. & Ju, J. 2008. The collection 5 MODIS burned area product — Global evaluation by comparison with the MODIS active fire product. *Remote Sensing of Environment*, 112(9):3690-3707.

Rutter, A.P. & Schauer, J.J. 2007. The Impact of Aerosol Composition on the Particle to Gas Partitioning of Reactive Mercury. *Environmental science & technology*, 41(11):3934-3939.

Rytuba, J.J. 2003. Mercury from mineral deposits and potential environmental impacts. *Environmental Geology*, 43:326-338.

Saiz-Lopez, A., Sitkiewicz, S.P., Roca-Sanjuán, D., Oliva-Enrich, J.M., Dávalos, J.Z., Notario, R., Jiskra, M., Xu, Y., Wang, F., Thackray, C.P., Sunderland, E.M., Jacob, D.J., Travnikov, O., Cuevas, C.A., Acuña, A.U., Rivero, D., Plane, J.M.C., Kinnison, D.E. & Sonke, J.E. 2018. Photoreduction of gaseous oxidized mercury changes global atmospheric mercury speciation, transport and deposition. *Nature Communications*, 9(1):4796.

Saiz-Lopez, A., Travnikov, O., Sonke, J.E., Thackray, C.P., Jacob, D.J., Carmona-García, J., Francés-Monerris, A., Roca-Sanjuán, D., Acuña, A.U., Dávalos, J.Z., Cuevas, C.A., Jiskra, M., Wang, F., Bieser, J., Plane, J.M.C. & Francisco, J.S. 2020. Photochemistry of oxidized Hg(I) and Hg(II) species suggests missing mercury oxidation in the troposphere. *Proceedings of the National Academy of Sciences*, 117(49): 30949-30956.

Schroeder, W.H. & Munthe, J. 1998. Atmospheric mercury—An overview. *Atmospheric Environment*, 32(5):809-822.

Scott, G.M. & Mdluli, T.N. 2012. The Minamata Treaty / Protocol: potential implications for South Africa. *Clean Air Journal = Tydskrif vir Skoon Lug*, 22(2):17-19.

Seigneur, C., Vijayaraghavan, K. & Lohman, K. 2006. Atmospheric mercury chemistry: Sensitivity of global model simulations to chemical reactions. *Journal of Geophysical Research: Atmospheres*, 111(D22).

Seinfeld, J.H. & Pandis, S.N. 2016. Atmospheric Chemistry and Physics: From Air Pollution to Climate Change. 3rd ed. Hoboken, NJ: Wiley & Sons, Inc.

Selin, N.E., Javob, D.J., Park, R.J., Yantosca, R.M., Strode, S., Jaeglé, L. & Jaffe, D. 2007. Chemical cycling and deposition of atmospheric mercury: Global constraints from observations. *Journal of Geophysical Research Atmospheres*, 112(2).

Si, L. & Ariya, P.A. 2008. Reduction of Oxidized Mercury Species by Dicarboxylic Acids (C2−C4): Kinetic and Product Studies. *Environmental science & technology*, 42(14):5150-5155.

Si, L. & Ariya, P.A. 2018. Recent Advances in Atmospheric Chemistry of Mercury. *Atmosphere*, 9(2):76.

Sigma-Aldrich. 2015. Materials safety data sheet: Mercury. http://www.sigmaaldrich.com/MSDS/MSDS/DisplayMSDSPage.do?country=ZA&language=en&productNumber=294594&brand=ALDRICH&PageToGoToURL=http%3A%2F%2Fwww.sigmaaldrich.com%2Fcatalog%2Fproduct%2Faldrich%2F294594%3Flang%3Den Date of access: 11 Sep. 17.

Slemr, F., Angot, H., Dommergue, A., Magand, O., Barret, M., Weigelt, A., Ebinghaus, R., Brunke, E.G., Pfaffhuber, K.A., Edwards, G., Howard, D., Powell, J., Keywood, M. & Wang, F. 2015. Comparison of mercury concentrations measured at several sites in the Southern Hemisphere. *Atmospheric Chemistry and Physics*, 15(6):3125-3133.

Slemr, F., Martin, L., Labuschagne, C., Mkololo, T., Angot, H., Magand, O., Magand, O., Garat, P., Ramonet, M. & Bieser, J. 2020. Atmospheric mercury in the Southern Hemisphere - Part 1: Trend and inter-annual variations in atmospheric mercury at Cape Point, South Africa, in 2007-2017, and on Amsterdam Island in 2012-2017. *Atmospheric Chemistry and Physics*, 20(13):7683-7692.

Sommar, J., Hallquist, M., Ljungström, E. & Lindqvist, O. 1997. On the Gas Phase Reactions Between Volatile Biogenic Mercury Species and the Nitrate Radical. *Journal of Atmospheric Chemistry*, 27(3):233-247.

South Africa. 2005. Notice of intention to declare the Vaal Triangle Air-shed Priority Area in terms of Section 18(1) of the National Environmental Management Air Quality Act 2004, (Act No 39 of 2004). (Notice 1007). *Government gazette*, 28132:3, 14 Oct.

South Africa. 2007. Notice of intention to declare the Highveld Priority Area in terms of Section 18(1) of the National Environmental Management Air Quality Act 2004, (Act No 39 of 2004). (Notice 396). *Government gazette*, 29864:3, 4 May.

South Africa. 2009. National Ambient Air Quality Standards. (Notice 1210). *Government gazette*, 32816:6, 24 Dec.

South Africa. 2012. Declaration of the Waterberg National Priority Area. (Notice 495). *Government gazette*, 35435:60, 15 Jun.

South Africa. 2018. The 2017 National Framework for Air Quality Management in the Republic of South Africa. (Notice 1144). *Government gazette*, 41996:109, 26 Oct.

Sprovieri, F., Pirrone, N., Bencardino, M., D'Amore, F., Carbone, F., Cinnirella, S., Mannarino, V., Landis, M., Ebinghaus, R. & Weigelt, A. 2016. Atmospheric mercury concentrations observed at ground-based monitoring sites globally distributed in the framework of the GMOS network. *Atmospheric Chemistry and Physics*, 16(18):11915-11935.

Stein, A.F., Draxler, R.R., Rolph, G.D., Stunder, B.J.B., Cohen, M.D. & Ngan, F. 2015. NOAA's HYSPLIT Atmospheric Transport and Dispersion Modeling System. *Bulletin of the American Meteorological Society*, 96(12):2059-2077.

Stetson, S.J., Gray, J.E., Wanty, R.B. & Macalady, D.L. 2009. Isotopic variability of mercury in ore, mine-waste calcine, and leachates of mine-waste calcine from areas mined for mercury. *Environmental science & technology*, 43(19):7331-7336.

Stohl, A. 1998. Computation, accuracy and applications of trajectories - A review and bibliography. *Atmospheric Environment*, 32(6):947-966.

Street, R.A. 2015. Emission accomplished: formal and informal mercury sources in South Africa. *Clean Air Journal = Tydskrif vir Skoon Lug*, 25(2):9-11.

Streets, D.G., Zhang, Q. & Wu, Y. 2009. Projections of Global Mercury Emissions in 2050. *Environmental science & technology*, 43(8):2983-2988.

Tang, W.-L., Liu, Y.-R., Guan, W.-Y., Zhong, H., Qu, X.-M. & Zhang, T. 2020. Understanding mercury methylation in the changing environment: Recent advances in assessing microbial methylators and mercury bioavailability. *Science of The Total Environment*, 714:136827.

Travnikov, O., Angot, H., Artaxo, P., Bencardino, M., Bieser, J., D'Amore, F., Dastoor, A., De Simone, F., Diéguez, M.D.C., Dommergue, A., Ebinghaus, R., Feng, X.B., Gencarelli, C.N., Hedgecock, I.M., Magand, O., Martin, L., Matthias, V., Mashyanov, N., Pirrone, N., Ramachandran, R., Read, K.A., Ryjkov, A., Selin, N.E., Sena, F., Song, S., Sprovieri, F., Wip, D., Wängberg, I. & Yang, X. 2017. Multi-model study of mercury dispersion in the

atmosphere: atmospheric processes and model evaluation. *Atmospheric Chemistry and Physics*, 17(8):5271-5295.

Tyson, P., Garstang, M. & Swap, R. 1996. Large-Scale Recirculation of Air over Southern Africa. *Journal of Applied Meteorology*, 35:2218-2236.

UNEP. 2017. At a glance: Minamata Convention on Mercury. http://www.mercuryconvention.org/Portals/11/documents/Awareness%20raising/FACT%20SHEETS/Minamata%20Convention%20on%20Mercury%20at%20a%20glance_COP1%202017.pdf Date of access: 10 December 2020.

Vakkari, V., Laakso, H., Kulmala, M., Laaksonen, A., Mabaso, D., Molefe, M., Kgabi, N., Beukes, J. & Laakso, L. 2011. New particle formation events in semi-clean South African savannah. *Clean Air Journal = Tydskrif vir Skoon Lug*, 20:20-24.

Vakkari, V., Kerminen, V.M., Beukes, J.P., Tiitta, P., van Zyl, P.G., Josipovic, M., Venter, A.D., Jaars, K., Worsnop, D.R. & Kulmala, M. 2014. Rapid changes in biomass burning aerosols by atmospheric oxidation. *Geophysical Research Letters*, 41(7):2644-2651.

Vakkari, V., Beukes, J.P., Dal Maso, M., Aurela, M., Josipovic, M. & van Zyl, P.G. 2018. Major secondary aerosol formation in southern African open biomass burning plumes. *Nature Geoscience*, 11:580-583.

van der Werf, G.R., Randerson, J.T., Giglio, L., van Leeuwen, T.T., Yang, C., Rogers, B.M., Mingquan, M., van Marle, M.J.E., Morton, D.C., Collatz, G.J., Yokelson, R.J. & Kasibhatla, P.S. 2017. Global fire emissions estimates during 1997–2016. *Earth System Science Data*, 9(2):697-720.

Van Loon, L., Mader, E. & Scott, S.L. 2000. Reduction of the Aqueous Mercuric Ion by Sulfite: UV Spectrum of HgSO3 and Its Intramolecular Redox Reaction. *The Journal of Physical Chemistry A*, 104(8):1621-1626.

Van Wilgen, B.W., Forsyth, G.G., De Klerk, H., Das, S., Khuluse, S. & Schmitz, P. 2010. Fire management in Mediterranean-climate shrublands: a case study from the Cape fynbos, South Africa. *Journal of Applied Ecology*, 47(3):631-638.

Velasco, A., Arcega-Cabrera, F., Oceguera-Vargas, I., Ramírez, M., Ortinez, A., Umlauf, G. & Sena, F. 2016. Global Mercury Observatory System (GMOS): measurements of atmospheric mercury in Celestun, Yucatan, Mexico during 2012. *Environmental Science and Pollution Research*, 23(17):17474-17483.

Venter, A.D., Vakkari, V., Beukes, J.P, van Zyl, P.G., Laakso, H., Mabaso, D., Tiitta, P., Josipovic, M., Kulmala, M., Pienaar, J. & Laakso, L. 2012. An air quality assessment in the industrialised western Bushveld Igneous Complex, South Africa. *South African Journal of Science*, 108(9/10):1059, 10 pages.

Venter, A.D., Beukes, J.P., van Zyl, P.G., Brunke, E., Labuschagne, C., Slemr, F., Ebinghaus, R. & Kock, H. 2015. Statistical exploration of gaseous elemental mercury (GEM) measured at Cape Point from 2007 to 2011. *Atmospheric Chemistry and Physics*, 15:10271-10280.

Venter, A.D., Beukes, J.P., van Zyl, P.G., Josipovic, M., Jaars, K. & Vakkari, V. 2016. Regional atmospheric Cr(VI) pollution from the Bushveld Complex, South Africa. *Atmospheric Pollution Research*, 7(5):762-767.

Venter, A.D., van Zyl, P.G., Beukes, J.P., Swartz, J.-S., Josipovic, M., Vakkari, V., Laakso, L. & Kulmala, M. 2018. Size-resolved characteristics of inorganic ionic species in atmospheric aerosols at a regional background site on the South African Highveld. *Journal of Atmospheric Chemistry*, 75(3):285-304.

Venter, M., Beukes, J.P., van Zyl, P.G., Vakkari, V., Virkkula, A., Josipovic, M., Kulmala, M. & Laakso, L. 2020. Six-year observations of aerosol optical properties at a southern African grassland savannah site. *Atmospheric Environment*, 230:117477.

Wang, Z. & Pehkonen, S.O. 2004. Oxidation of elemental mercury by aqueous bromine: atmospheric implications. *Atmospheric Environment*, 38(22):3675-3688.

Wilson, M. 2020. Cinnabar. https://www.mindat.org/photo-349626.html Date of access: 9 December 2020.

Ye, Z., Mao, H., Lin, C.J. & Kim, S.Y. 2016. Investigation of processes controlling summertime gaseous elemental mercury oxidation at midlatitudinal marine, coastal, and inland sites. *Atmospheric Chemistry and Physics*, 16(13):8461-8478.

Yin, X., Zhou, W., Kang, S., de Foy, B., Yu, Y., Xie, J., Sun, S., Wu, K. & Zhang, Q. 2020. Latest observations of total gaseous mercury in a megacity (Lanzhou) in northwest China. *Science of The Total Environment*, 720:137494.

Zannetti, P. 1990. 'Chapter 10: Dry and Wet Deposition', in *Air Pollution Modeling: Theories, Computational Methods and Available Software*, Springer US, Boston. p. 249-262.

Zhao, L., Meng, B. & Feng, X. 2020. Mercury methylation in rice paddy and accumulation in rice plant: A review. *Ecotoxicology and Environmental Safety*, 195:110462.